Master's thesis

Dynamical Mean-Field Theory + Numerical Renormalization Group Study of Strongly Correlated Systems with Spin-Orbit Coupling

Gianni Del Bimbo

Chair of Theoretical Solid State Physics
Faculty of Physics
Ludwig-Maximilians-Universität München

Supervisors:
Prof. Dr. Jan von Delft
Dr. Seung-Sup B. Lee

Munich, February 6, 2020

Masterarbeit

Dynamische Molekularfeldtheorie + Numerische Renormierungsgruppe für stark korrelierte Elektronensysteme mit Spin-Bahn-Kopplung

Gianni Del Bimbo

Lehrstuhl für Theoretische Festkörperphysik
Fakultät für Physik
Ludwig-Maximilians-Universität München

Betreuer:
Prof. Dr. Jan von Delft
Dr. Seung-Sup B. Lee

München, den 6. Februar 2020

Declaration:

I hereby declare that this thesis is my own work, and that I have not used any sources and aids other than those stated in the thesis.

München, February 6, 2020

Gianni Del Bimbo

Acknowledgements

I am thankful to Jan von Delft for his advice and help. Many thanks to Seung-Sup B. Lee for his guidance and patience in dealing with my questions and doubts. I would also like to thank Elias and Fabian for many helpful and instructive discussions. Special thanks to Sebastian for all the IT support he gave me in times of technical issues. Thanks to the funniest and merriest office fellows, David, Felix and Santiago (alphabetically but not time-ordered). I could not hope for better companions for this journey. I will always keep fond memories of the Büro A415. I thank my family for the unconditional support. Thank you G̃iulia.

Contents

Introduction

Strongly correlated systems have fascinated physicists for many decades and still represent a prominent topic in condensed matter physics. In these systems strong correlations between electrons give rise to a plethora of fascinating many-body phenomena as metal-insulator transition [29], high-temperature superconductivity (for example in cuprates [5]), colossal magnetoresistance (for example in manganites [39]). An exemplary family of strongly correlated materials is that of transition-metal oxides, where a transition-metal atom is typically embedded in an octahedral structure of oxygen atoms. In such materials the d-orbital degeneracy of the metallic atom is partially lifted so that a three-band model can be adopted. In this context the new paradigm of "Hund metals" emerges, in which the correlations are driven by the Hund coupling rather than the Coulomb interaction [2]. Examples of such materials are ruthenates and iron-based superconductors (iron pnictides and chalcogenides). In particular, the relevance of spin-orbit coupling (SOC) has recently attracted much interest. In weakly correlated materials SOC plays a central role for topological insulators [14], in Mott insulators it influences the magnetic exchange leading to rich spin-orbital physics [18], in heavy-fermion compounds it selects the multiplet structure [28]. In contrast, the effects of SOC in strongly correlated metals are far less explored and understood. Since SOC strength increases with the atomic number, its effects become more prominent for elements of $4d$ and $5d$ series. For example, iridates have recently drawn much interest, for the large SOC can give rise to novel phases such as topological superconductivity [19]. The situation is more complex in $4d$ compounds (e.g. ruthenates) where all the energy scales are comparable (Coulomb repulsion, Hund interaction, SOC and hopping integral) [40, 44] and an intricate interplay is at work. In recent years, a number of studies have tried to capture the physics arising in these multiorbital materials, both from a real-material perspective [22] and from a model one [16, 21, 52], showing a rich interplay between correlations and SOC and possible novel phases [16, 21, 52].

The goal of this thesis is to analyze the subject from a model viewpoint, using single-site Dynamical Mean-Field Theory (DMFT) [1], a well-established method to investigate strongly correlated systems, where a lattice site is singled out and embedded in an self-consistently determined environment, representing the interplay between the rest of the solid and the site. The problem is thus mapped onto a quantum-impurity model which in turn is solved employing the Numerical Renormalization Group (NRG) method [38]. We use a state-of-the-art NRG implementation developed in our group by A. Weichselbaum and S.-S. B. Lee, which combines efficiency in exploiting symmetries, especially important for multi-band models [57, 23], and high-resolution power for computing spectral functions on real frequencies. [42].

The thesis is structured as follows: Chapter 1 contains an overview of the idea and concepts of single-site DMFT. In Chapter 2 the standard NRG procedure is introduced, following the review by R. Bulla, T.A. Costi, and T. Pruschke [37]. Although these first

two chapters provide quite standard presentations, they serve the purpose to provide a brief introduction of the methods for the reader not familiar with them. In Chapter 3 the adopted three-band model is presented and the role of SOC in d-systems explained. In Chapter 4 we present and analyze our NRG and DMFT results. Finally, an outlook on our results and possible future research directions are discussed.

Chapter 1

Dynamical Mean-Field Theory

The Dynamical Mean-Field Theory (DMFT) is one of the most successful non-perturbative methods to investigate strongly correlated systems, for it retains the proper competition between the kinetic energy and the electronic interactions. Two insights paved the way to the development of this powerful theory. First, the finding that in infinite dimensions all the contributions to the self-energy are purely local. Second, the construction of a mean-field theory, dynamical in nature, which allows to map self-consistently the correlated lattice problem onto a quantum-impurity model, which is solved numerically and hence provides important properties of the original lattice problem. This procedure opened new lines of research in the study of strongly correlated systems, with important applications to real materials. A detailed review of DMFT is given by A. Georges, G. Kotliar, W. Krauth and M.J. Rozenberg in [1].

1.1 Hubbard model in infinite dimensions

Following the historical development of DMFT, we present how the first key idea was introduced through the study of the Hubbard model in infinite dimensions, that is the scaling of the hopping term in the $d \to \infty$ limit [32, 53]. We consider the one-band, spin-1/2 model, i.e. the simplest model describing interacting electrons in a solid. In this model the interaction between the electrons is assumed to be so strongly screened that it is taken as purely local. The Hamiltonian on a cubic lattice in d dimensions is the following (to keep the notation light we omit hats for operators and set $\hbar = k_B = 1$ throughout)

$$H = H_{kin} + H_{int} - \mu N = -\sum_{\langle i,j\rangle,\sigma} t_{i,j}\, c^{\dagger}_{i,\sigma} c_{j,\sigma} + U \sum_{i} n_{i,\uparrow} n_{i,\downarrow} - \mu \sum_{i,\sigma} n_{i,\sigma} \tag{1.1}$$

where $\sum_{\langle i,j\rangle}$ denotes a sum over pairs of nearest neighbors, $c^{(\dagger)}_{i,\sigma}$ the annihilation (creation) operators of a conduction electron at site i with spin σ, $n_{i,\sigma} = c^{\dagger}_{i,\sigma} c_{i,\sigma}$ the number operator. The parameter U is the on-site Coulomb repulsion, μ is the chemical potential and $t_{i,j}$ is the hopping amplitude (overlap integral between Wannier functions, representing localized orbitals). For simplicity, in the following we consider the hopping to be site-independent $t_{i,j} = t$. The Fourier transform of H_{kin} gives

$$H_{kin} = \sum_{\boldsymbol{k},\sigma} \epsilon_{\boldsymbol{k}} n_{\boldsymbol{k},\sigma} \tag{1.2}$$

where $n_{\boldsymbol{k},\sigma}$ is the momentum distribution operator. The number of neighbors is called coordination number z and is $z = 2d$ for a hypercubic lattice.
The tight-binding dispersion relation reads (lattice spacing $\equiv 1$)

$$\epsilon_k = -2t \sum_{\alpha=1}^{d} \cos k_\alpha \,. \tag{1.3}$$

In the $d \to \infty$ limit, in order to retain the full competition between the kinetic energy and the electronic interaction, we need to perform a proper scaling of the Hamiltonian. The interaction part and the chemical potential part, being purely local, are independent of the lattice structure and hence of the number of neighbors z. Instead, the kinetic energy per site scales with z and so diverges in the infinite limit. Therefore, we require the width of the non-interacting density of states (DOS),

$$\rho_0(\epsilon) = \frac{1}{N_B} \sum_{\boldsymbol{k}} \delta(\epsilon - \epsilon_{\boldsymbol{k}}) = \int_{-\pi}^{\pi} \frac{d\boldsymbol{k}}{(2\pi)^d}\, \delta(\epsilon - \epsilon_{\boldsymbol{k}}) \tag{1.4}$$

to be independent of d (we replace the sum by an integral in the thermodynamic limit). A measure of the width of the DOS is its variance,

$$\sigma^2 = \int_{-\infty}^{\infty} d\epsilon\, \rho_0(\epsilon)\, \epsilon^2 = 2t^2 d \tag{1.5}$$

so that, in order to keep the width finite, we demand that the hopping amplitude scales like

$$t = \frac{t^*}{\sqrt{2d}} = \frac{t^*}{\sqrt{z}} \tag{1.6}$$

with t^* constant. We can also derive this scaling by using the central limit theorem [32, 24]. In fact, the DOS can be interpreted as the probability density for finding $\epsilon = \epsilon_{\boldsymbol{k}}$ for a random choice of $\boldsymbol{k} = (k_1, ..., k_d)$. One can construct the random variables $X_\alpha = \sqrt{2}\cos(k_\alpha)$, with zero mean and unit variance, which are uniformly distributed in the interval $[-\pi, \pi]$. Then the distribution function of $X_d = \frac{1}{\sqrt{d}} \sum_{\alpha=1}^{d} X_\alpha$ converges in law to a Gaussian distribution, again with zero mean and unit variance. If we consider the density of states $\rho_0(\epsilon)$ as the distribution function of the random variable $\sqrt{2d}\, t X_d$, we obtain the following Gaussian

$$\rho_0(\epsilon) \overset{d\to\infty}{\longrightarrow} \frac{1}{2t\sqrt{\pi d}} \exp\left[-\left(\frac{\epsilon}{2t\sqrt{d}} \right)^2 \right]. \tag{1.7}$$

Unless t is scaled like (1.6) this Gaussian DOS will become arbitrarily broad and featureless in the $d \to \infty$ limit,

$$\rho_0^\infty(\epsilon) = \frac{1}{t^*\sqrt{2\pi}} \exp\left[-\frac{1}{2}\left(\frac{\epsilon}{t^*} \right)^2 \right], \qquad t = \frac{t^*}{\sqrt{2d}}\,. \tag{1.8}$$

The rescaled Hubbard Hamiltonian

$$H = -\frac{t^*}{\sqrt{z}} \sum_{\langle i,j\rangle,\sigma} c_{i,\sigma}^\dagger c_{j,\sigma} + U \sum_i n_{i,\uparrow} n_{i,\downarrow} \tag{1.9}$$

has a well-defined $z \to \infty$ (or $d \to \infty$) limit and retains the proper competition between H_{kin} and H_{int}.
The scaling can also be derived within a position-space formulation and we will see how this leads to simplifications of many-body diagrammatic theory [53]. To show this we consider non-interacting electrons at $T = 0$, then the expectation value of the kinetic energy is given by

$$E^0_{kin} = -t \sum_{\langle i,j\rangle,\sigma} g^0_{ij,\sigma} \tag{1.10}$$

where $g^0_{ij,\sigma} = \langle c^\dagger_{i,\sigma} c_{j,\sigma}\rangle_0$ is the one-particle density matrix. This quantity may be interpreted as the amplitude for transitions between sites i and j. Therefore the square of its absolute value is proportional to the probability for a particle hopping from site j to site i. In the case of nearest-neighbor hopping on a lattice with coordination number z this implies $|g^0_{ij,\sigma}|^2 \sim \mathcal{O}(\frac{1}{z})$. For nearest neighbors on the hypercubic lattice (where $z = 2d$) we then have

$$g^0_{ij,\sigma} \sim \mathcal{O}\left(\frac{1}{\sqrt{d}}\right). \tag{1.11}$$

Since the sum over all nearest neighbors of a site j in (1.10) is of order $\mathcal{O}(d)$, the hopping amplitude t must scale as in (1.6) to keep the kinetic energy finite in the $z, d \to \infty$ limit. It can be shown [36, 31] that, for general i and j, one obtains

$$g^0_{ij,\sigma} \sim \mathcal{O}\left(\frac{1}{d^{\frac{\|\boldsymbol{R}_i - \boldsymbol{R}_j\|}{2}}}\right) \tag{1.12}$$

where $\boldsymbol{R}_i$ is the lattice vector of site i and $\|\boldsymbol{R}\| = \sum_{\alpha=1}^{d} |R_\alpha|$ is the length of $\boldsymbol{R}$ in the "Manhattan metric", where particles only hop horizontally and vertically, never diagonally.
It is important to note that, although $g^0_{ij,\sigma} \sim \mathcal{O}\big(1/\sqrt{d}\big)$ vanishes for $d \to \infty$, the off-diagonal elements of $g^0_{ij,\sigma}$ still contribute, since the particles may hop to d nearest neighbors with amplitude $t^*/\sqrt{2d}$. In the limit of infinite dimensions the particles are hence not localized, but still mobile.

1.2 Green function and self-energy

The central quantity in DMFT for studying the equilibrium properties of a correlated electronic system is the one-particle retarded Green's function

$$G^R_{\alpha\beta}(t) = -i\,\Theta(t)\big\langle\{c_\alpha(t)c^\dagger_\beta(0)\}\big\rangle \tag{1.13a}$$

$$G^R_{\alpha\beta}(\omega) = \int_{-\infty}^{\infty} \frac{dt}{2\pi} e^{i\omega t}\, G^R_{\alpha\beta}(t) \tag{1.13b}$$

with α and β being general momentum or site indices, including also spin and orbital quantum numbers. The operator $c_\alpha(t) = e^{iHt} c_\alpha e^{-iHt}$ is time-evolved in the Heisenberg picture. The retarded Green function can be written in its spectral representation

$$G^R_{\alpha\beta}(\omega) = \int_{-\infty}^{\infty} d\omega' \frac{A_{\alpha\beta}(\omega')}{\omega + i0^+ - \omega'} \tag{1.14}$$

where the spectral function $A_{\alpha\beta}(\omega)$ is given by its Lehmann representation as

$$A_{\alpha\beta}(\omega) = \frac{1}{Z}\sum_{n,m}\langle n|c_\beta^\dagger|m\rangle\,\langle m|c_\alpha|n\rangle\left(e^{-\beta E_m} - e^{-\beta E_n}\right)\delta(\omega-(E_n-E_m)) \tag{1.15}$$

where Z is the partition function and E_n the eigenvalues and $|n\rangle$ the eigenstates of the Hamiltonian H. Note that $A_{\alpha\alpha}(\omega) \geq 0$. From the pole structure of (1.14) it follows that

$$A_{\alpha\beta}(\omega) = -\frac{1}{\pi}\,\mathrm{Im}\,G^R_{\alpha\beta}(\omega)\,. \tag{1.16}$$

We note that the argument of Green or spectral functions is never purely real, but it is always implied $\omega \equiv \omega + i0^+$.
Of particular importance is the local Green function (we omit the superscript R)

$$G_{ii,\sigma}(\omega) = G_\sigma(\omega) = \frac{1}{N_B}\sum_{\boldsymbol{k}} G_{\boldsymbol{k},\sigma}(\omega) \tag{1.17a}$$

$$A_{ii,\sigma}(\omega) = A_\sigma(\omega) = -\frac{1}{\pi}\,\mathrm{Im}\,G_\sigma(\omega) \tag{1.17b}$$

where lattice, spin and momentum indices are explicitly adopted and translation invariance assumed. The quantity $A_\sigma(\omega)$ is called local density of states and it can be used to deduce transport properties as we will see later. It also obeys the sum rule

$$\int_{-\infty}^{\infty} d\omega A_\sigma(\omega) = 1 \tag{1.18}$$

For non-interacting systems, the free Green function and the free density of states are given by

$$G^{(0)}_{\boldsymbol{k},\sigma}(\omega) = \frac{1}{\omega+\mu-\epsilon_{\boldsymbol{k}}} \tag{1.19}$$

$$\rho_0(\omega) = A^{(0)}_\sigma(\omega) = \frac{1}{N_B}\sum_{\mathbf{k}}\delta(\omega-\epsilon_{\boldsymbol{k}}) \tag{1.20}$$

For interacting systems we define the self-energy as the difference between free and interacting reciprocal Green functions

$$G_{\boldsymbol{k},\sigma}(\omega)^{-1} = G^{(0)}_{\boldsymbol{k},\sigma}(\omega)^{-1} - \Sigma_{\boldsymbol{k},\sigma}(\omega) \tag{1.21a}$$

$$G_{\boldsymbol{k},\sigma}(\omega) \equiv \langle c_{\boldsymbol{k},\sigma}||c^\dagger_{\boldsymbol{k},\sigma}\rangle_\omega = \frac{1}{\omega+\mu-\epsilon_{\boldsymbol{k}}-\Sigma_{\boldsymbol{k},\sigma}(\omega)}\,. \tag{1.21b}$$

For a translationally invariant system, the self-energy and the Green function are thus diagonal in momentum space. Finally, we note that we are dealing with retarded Green functions, which are causal and hence analytic in the upper half-plane, so that $\mathrm{Im}\,\Sigma_{\boldsymbol{k},\sigma}(\omega) < 0$, implying that the poles of $G_{\boldsymbol{k},\sigma}(\omega)$ lie in lower half-plane.

1.3 Local nature of self-energy

In this section we show how the scaling in the limit $z \to \infty$ leads to simplifications in the many-body perturbation treatment. By construction the kinetic energy is finite and can be written as

$$E_{kin} = \sum_{\langle i,j\rangle,\sigma}\frac{t^*}{\sqrt{2d}}\langle c^\dagger_{i,\sigma}c_{j,\sigma}\rangle = \lim_{t\to 0^+}\sum_{\langle i,j\rangle,\sigma}\frac{t^*}{\sqrt{2d}}\int_{-\infty}^{\infty}\frac{d\omega}{2\pi i}\,e^{i\omega t}\,G_{ij,\sigma}(\omega) = \mathcal{O}(d^0)\,. \tag{1.22}$$

Since the sum over the nearest neighbors of a given site i gives a factor of $z = 2d$, we see that $G_{ij,\sigma}(\omega)$ has to scale like

$$G_{ij,\sigma}(\omega) \sim \mathcal{O}\left(\frac{1}{\sqrt{d}}\right) \tag{1.23a}$$

$$G_{ii,\sigma}(\omega) \sim \mathcal{O}(d^0)\,. \tag{1.23b}$$

More generally, when we consider models with hopping beyond nearest neighbors we have that

$$G_{ij,\sigma}(\omega) \sim \mathcal{O}\left(d^{-\frac{1}{2}\|\boldsymbol{R}_i - \boldsymbol{R}_j\|}\right) \tag{1.24a}$$

$$G_{ii,\sigma}(\omega) \sim \mathcal{O}(d^0) \tag{1.24b}$$

i.e. the off-diagonal Green function rapidly decays with distance.
We now consider the skeleton expansion of the self-energy

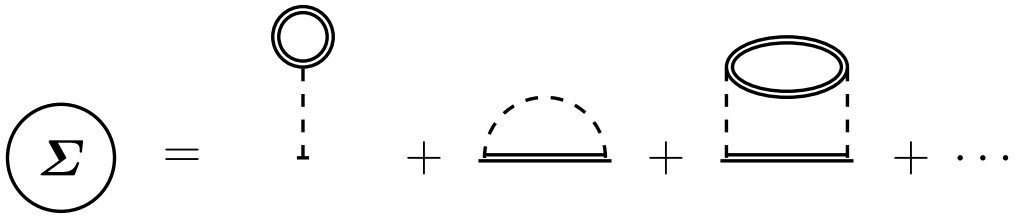

Figure 1.1: Skeleton expansion of Σ. Figure from [24].

where the double lines denote the full interacting Green propagators and the dashed lines the local interaction vertices. Since in the Hubbard model the full interacting propagator scales like (1.23a), we see that, for two vertices connected by three full propagators in the $d \to \infty$ limit, we obtain

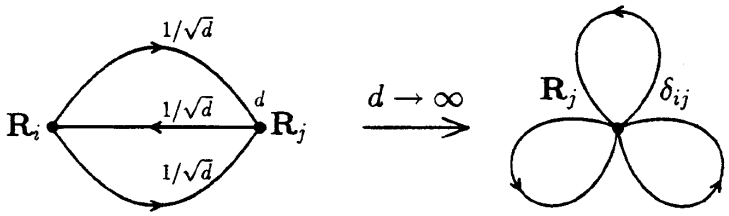

Figure 1.2: Example of second order diagram from the skeleton expansion of the self-energy. The total contribution of the three full propagators is of order $d^{-\frac{3}{2}}$ while the sum over the nearest neighbors yields a factor of order d. Therefore the second order diagram contributes a factor of $d^{-\frac{1}{2}}$ and collapses in infinite dimensions. Figure from [53].

From figure (1.2) we see that the second order diagrams in the self-energy expansion collapse in the $d \to \infty$ limit and the same argument applies to higher order diagrams which collapse even faster (they have more than three full propagators).
Therefore the self-energy Σ becomes purely local in infinite dimensions, that is site-diagonal in real space and k-independent in momentum space

$$\Sigma_{ij,\sigma}(\omega) \overset{d\to\infty}{\longrightarrow} \Sigma_\sigma(\omega)\delta_{ij} \tag{1.25a}$$

$$\Sigma_{\boldsymbol{k},\sigma}(\omega) \overset{d\to\infty}{\longrightarrow} \Sigma_\sigma(\omega)\,. \tag{1.25b}$$

This leads to tremendous simplifications in that the most important obstacle for actual diagrammatic calculations in finite dimensions $d \geq 1$, that is the integration over intermediate momenta, is removed in $d \to \infty$. Yet, being the self-energy still frequency dependent, it completely accounts for temporal quantum fluctuations, which are at the core of the physics of strongly correlated materials. However, it freezes out spatial fluctuations, so that we cannot access the non-local interactions of the lattice (there exist cluster extentions of DMFT which take short-ranged interactions into account [33, 34, 11]). This simplified form of the Σ also has a direct consequence on the retarded Green function,

$$G_{\boldsymbol{k},\sigma}(\omega) = \frac{1}{\omega + \mu - \epsilon_{\boldsymbol{k}} - \Sigma_\sigma(\omega)} = G^{(0)}_{\boldsymbol{k},\sigma}\big(\omega - \Sigma_\sigma(\omega)\big)\,. \tag{1.26}$$

Summing over $\boldsymbol{k}$ yields the local Green function

$$G_\sigma(\omega) = \int \frac{d\boldsymbol{k}}{(2\pi)^d} \frac{1}{\omega + \mu - \epsilon_{\boldsymbol{k}} - \Sigma_\sigma(\omega)} \tag{1.27}$$

$$= \int_{-\infty}^{\infty} d\epsilon \, \frac{\rho_0(\epsilon)}{\omega + \mu - \epsilon - \Sigma_\sigma(\omega)} \tag{1.28}$$

where in the last equation we introduce the non-interacting density of states. We note, however, that the model is not reduced to a purely local one as the hopping between sites is still retained via the momentum-dependent dispersion relation $\epsilon_{\boldsymbol{k}}$.

1.3.1 Non-interacting density of states: the Bethe lattice

In this subsection we discuss the particular DOS used in this thesis: the Bethe lattice. As seen in Eqs. (1.27,1.28), the specific features of the lattice are taken into account via the non-interacting DOS and the dispersion relation (also via the parameters in the model, like Coulomb strength and number of orbitals). In model calculations it is common to use the infinite limit of non-interacting DOS as an approximation to finite-dimensional lattices [53]. An important lattice, often used within DMFT and also in this work, is the infinite Caley tree, also called Bethe lattice (see Fig. 1.3).
In the limit of infinite neighbors $z \to \infty$ the Bethe DOS is semi-elliptic,

$$\rho_0^{Bethe}(\epsilon) = \frac{2}{\pi D}\sqrt{1 - \left(\frac{\epsilon}{D}\right)^2}, \quad \epsilon \in [-D, D] \tag{1.29}$$

where $D = 2t\sqrt{z}$ is the half-bandwidth of the DOS and t the rescaled hopping that scales as $\propto 1/\sqrt{z}$.
The reason why the Bethe lattice is often adopted is that it yields a closed analytic form of the local Green function (1.28), namely

$$G_\sigma(\omega) = \int_{-\infty}^{\infty} d\epsilon \, \frac{\rho_0^{Bethe}(\epsilon)}{\underbrace{\omega + \mu - \Sigma_\sigma(\omega)}_{\equiv \xi} - \epsilon} = \frac{2}{D^2}\Big(\xi - i\sqrt{D^2 - \xi^2}\Big)\,. \tag{1.30}$$

If one adopts Bethe lattice the numerical integration of (1.28) can then be avoided.

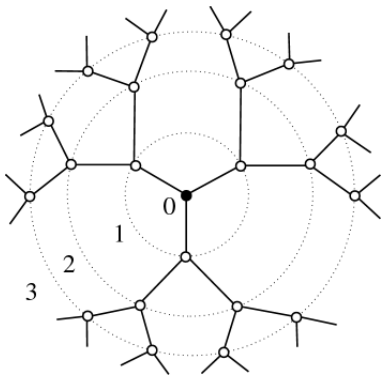

Figure 1.3: The Bethe lattice with $z = 3$, illustrated in successive shells.

1.4 Effective impurity problem

We have seen that in the infinite-dimensional limit the effects due to interactions are purely local. Still we have to find a way to determine the self-energy and in turn the local Green function of the lattice. The answer, which established the basic framework of DMFT, was given by Georges and Kotliar [12]: the lattice model can be mapped onto an effective quantum (Anderson) impurity model in a self-consistent fashion. The impurity model inherits the same local interactions of a lattice site and is embedded in a non-interacting electronic bath that is self-consistently determined so to best represent the original environment of the site (Fig. 1.4). Since the local interactions are the same and only local effects enter the self-energy we have (skipping the spin index for simplicity)

$$\Sigma_{latt}(\omega) = \Sigma_{imp}(\omega) \equiv \Sigma(\omega) \tag{1.31}$$

where the subscripts *latt* and *imp* refer to lattice and impurity quantities, respectively. The coupling between the impurity and the bath is described by the hybridization function $\Delta(\omega)$, whose energy-dependence encodes the correlation effects of the rest of the lattice (the site assigned to the impurity being excluded). The impurity Green function, with the same self-energy $\Sigma(\omega)$ and chemical potential μ (via the mapping the local energy level ϵ_d of the impurity is equal to minus the chemical potential, $\epsilon_d = -\mu$), reads

$$G_{imp}(\omega) = \frac{1}{\omega - \epsilon_d - \Sigma(\omega) - \Delta(\omega)} \tag{1.32}$$

Hence we can determine the dynamics of the lattice, i.e. the local lattice Green function, by solving the impurity problem, i.e. determining the impurity Green function, so that the mapping onto the impurity problem can be written as

$$G_{latt}(\omega) \stackrel{!}{=} G_{imp}\,. \tag{1.33}$$

The effective impurity problem corresponding to the single-band Hubbard model is the single impurity Anderson model (SIAM) [12], where the impurity, H_{imp}, is coupled to the

bath, H_{bath}, via the hybridization Hamiltonian H_{hyb}, ($k \equiv \boldsymbol{k}$)

$$\begin{aligned} H_{SIAM} &= H_{imp} + H_{bath} + H_{hyb} \\ H_{imp} &= \sum_{\sigma} \epsilon_d \, d_{\sigma}^{\dagger} d_{\sigma} + U n_{\uparrow} n_{\downarrow} \\ H_{bath} &= \sum_{k,\sigma} \epsilon_k \, c_{k,\sigma}^{\dagger} c_{k,\sigma} \\ H_{hyb} &= \sum_{k,\sigma} V_k \left(c_{k,\sigma}^{\dagger} d_{\sigma} + d_{\sigma}^{\dagger} c_{k,\sigma} \right) \end{aligned} \tag{1.34}$$

where $d_{\sigma}^{(\dagger)}$ annihilates (creates) an electron with spin $\sigma = \uparrow, \downarrow$ at the impurity site, $c_{k,\sigma}^{(\dagger)}$ are the corresponding annihilation (creation) operators for the non-interacting fermionic bath and the hybridization between the impurity and the bath is given by the hopping amplitudes V_k.
The effect of the environment on the impurity is fully encoded in the hybridization function

$$\Delta(\omega) = \sum_{k} \frac{V_k^2}{\omega - \epsilon_k} \, . \tag{1.35}$$

Since $\Delta(\omega)$ is causal, i.e. analytic in the upper complex half-plane, its real part can be derived from the imaginary part via the Kramers-Kronig relations, so it is sufficient to consider its imaginary part

$$\Gamma(\omega) = -\operatorname{Im} \Delta(\omega) = \pi \sum_{k} V_k^2 \, \delta(\omega - \epsilon_k) \tag{1.36}$$

which plays an analogous role of the Weiss field in the classical mean-field theory [6]. The hybridization function $\Gamma(\omega)$ is frequency-dependent and hence 'dynamical', but it is not known *a priori*. In fact it has to be determined self-consistently in order to obtain the impurity Green function and, consequently, the local lattice Green function.

1.5 Self-consistent DMFT equations

The mapping procedure allows to get a closed set of DMFT equations that can be solved iteratively. By using the self-consistent condition Eq. (1.33) and Eq. (1.32) we obtain

$$G_{latt}(\omega)^{-1} + \Sigma(\omega) = \omega + \mu - \Delta(\omega) = G_{imp}^{(0)}(\omega)^{-1} \tag{1.37}$$

that leads to a simple expression for the hybridization function

$$\Gamma(\omega) = -\operatorname{Im} \Delta(\omega) = \operatorname{Im}(G_{latt}(\omega)^{-1} + \Sigma(\omega)) \, . \tag{1.38}$$

From Eq. (1.31), $\Sigma_{latt}(\omega) = \Sigma_{imp}(\omega) \equiv \Sigma(\omega)$, we can devise an iterative procedure to solve the DMFT equations (Fig. 1.5):

(i) start with some guess for $\Gamma_{in}(\omega)$

(ii) solve the impurity problem to determine $\Sigma(\omega)$

(iii) compute $G_{latt} = \int_{-\infty}^{\infty} d\epsilon \, \frac{\rho_0(\epsilon)}{\omega + \mu - \epsilon - \Sigma(\omega)}$

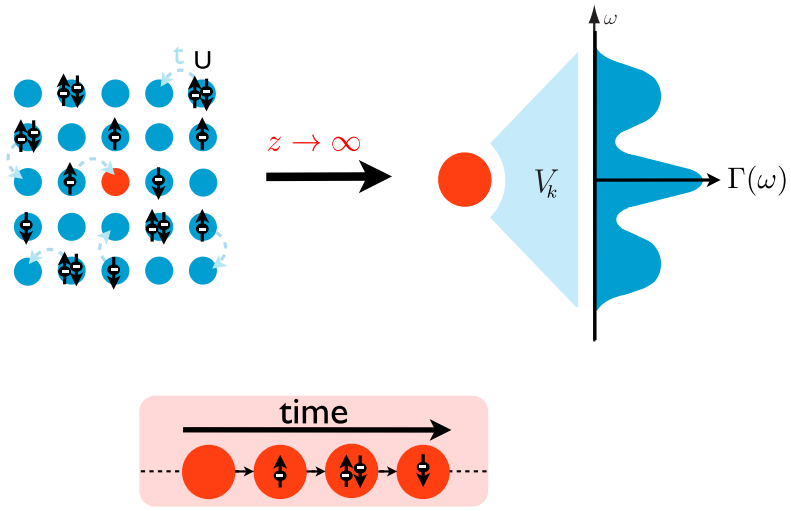

Figure 1.4: One site from the lattice on the left (representing the single-band Hubbard model) is singled out ($z \to \infty$ limit) and embedded into an effective bath on the right, which is self-consistently determined. The effect of the bath on the impurity is described by the hybridization function $\Gamma(\omega)$. The red box illustrates the fact that the local quantum fluctuations are taken in full account. Figure from [48].

(iv) update the hybridization function $\Gamma_{out}(\omega) = \mathrm{Im}(G_{latt}(\omega)^{-1} + \Sigma(\omega))$

(v) repeat from step (ii) until convergence, that is until $|\Gamma_{in}(\omega) - \Gamma_{out}(\omega)| < \delta$, where the tolerance δ is often set to 10^{-3}.

The central point now is how accurately and efficently we can solve the impurity problem, which is still a non-trivial complex many-body problem. In this thesis, as said before, we use the Bethe DOS which allows to avoid the numerical integration of step (iii) and to find a direct relation between the hybridization function and the lattice spectral function [41],

$$\begin{aligned} G_{latt}(\omega) = \frac{2}{D^2}\left(\xi - i\sqrt{D^2-\xi^2}\right) &\stackrel{!}{=} G_{imp} = \frac{1}{\xi - \Delta(\omega)} \\ \frac{D^2}{2\left(\xi - i\sqrt{D^2-\xi^2}\right)} &= \xi - \Delta(\omega) \\ \frac{\xi - i\sqrt{D^2-\xi^2}}{2} &= \xi - \Delta(\omega) \\ \implies \Delta(\omega) = \frac{\left(\xi - i\sqrt{D^2-\xi^2}\right)}{2} &= \frac{D^2}{4}\, G_{latt}(\omega)\,. \end{aligned} \tag{1.39}$$

Therefore, since $\Gamma(\omega) = -\,\mathrm{Im}\,\Delta(\omega)$ and $A(\omega) = -\frac{1}{\pi}\,\mathrm{Im}\,G_{latt}(\omega)$, we get

$$\frac{\Gamma(\omega)}{\pi} = \frac{D^2}{4}\, A(\omega)\,. \tag{1.40}$$

Over the past decades many techniques to solve quantum impurity problems have become available. Quantum Monte Carlo (QMC) methods are widely spread [15] and the continuous time formulation (CTQMC) is particularly used for solving quantum impurity problems [9]. Its main advantages are that it is numerically exact (in the statistical sense), its scaling to multi-orbital models is not so disadvantageous and is easily parallelizable.

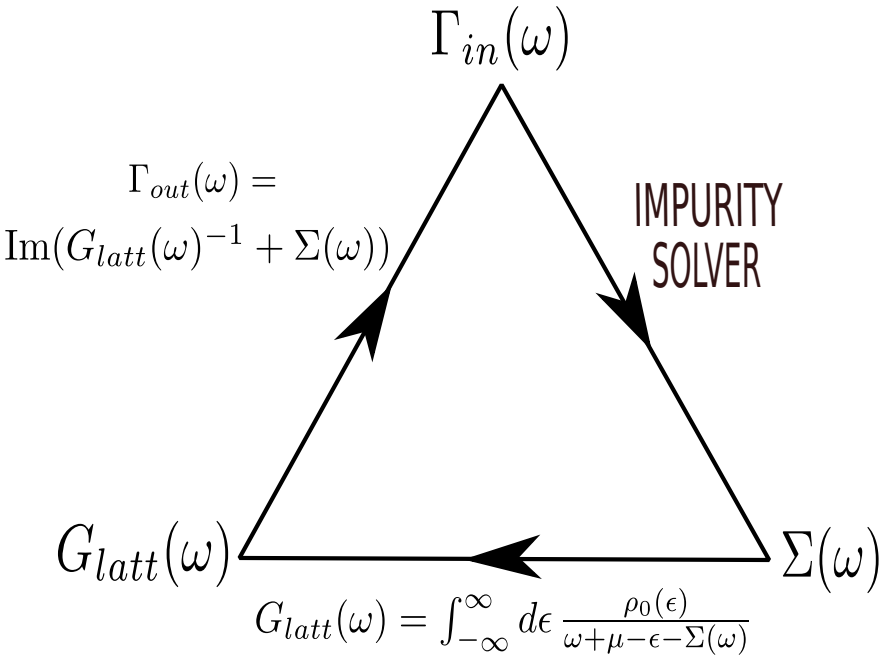

Figure 1.5: Illustration of the DMFT self-consistent procedure.

Among its drawbacks is the need for analytic continuation (QMC algorithms provide solutions on the imaginary Matsubara axis) which is numerically ill-posed and hinder the reliability and precision of the spectra. In addition, low temperatures within QMC methods are numerically quite expensive and subject to the so-called "sign problem" which prevents the solutions of certain multi-orbital problems due to the exponential increase in the sampling complexity. Other two popular methods are Exact Diagonalization (ED) [27] and DMRG [45, 8]. A number of analytical approximated methods are also available, like the iterated perturbation theory or the noncrossing approximation (for example see the references within [1]). In this thesis we use the Numerical Renormalization Group (NRG) method developed by Wilson [59]. It is a well-established method for solving quantum impurity problems. It has the advantage to compute the quantities of interest directly on the real frequency axis and can reach arbitrarily low energies/temperatures. Its main drawback is the poor scaling in multi-orbital models. However our group can rely on an extremely powerful NRG code (developed by A. Weichselbaum and S.-S.B. Lee), which is able to deal efficiently with complex systems in the context of symmetries, both Abelian and non-Abelian [56]. By exploiting the maximum number of symmetries, calculations for multi-orbital models become feasible too. In the next chapter we will briefly introduce the basics and concepts of NRG.

Chapter 2

Numerical Renormalization Group

The Numerical Renormalization Group (NRG) was developed by K.G. Wilson in the 1970's for the solution of the Kondo problem in a non-perturbative fashion. In this problem, a single magnetic impurity is coupled with the electronic conduction band of a nonmagnetic metal [59]. Since then it has been improved to become a reliable and powerful method to solve impurity problems [38]. In this chapter we will summarize the basic procedure of NRG, following the review by R. Bulla, T.A. Costi, and T. Pruschke [38].

The class of fermionic Hamiltonians which can be solved with NRG can be written in the following way

$$H = H_{imp} + H_{bath} + H_{hyb} \tag{2.1}$$

where the impurity Hamiltonian H_{imp} can contain any local interaction. Since the impurity is described by a small number of degrees of freedom, it can be diagonalized exactly. The non-interacting electronic bath can be described by

$$H_{bath} = \sum_{\mu=1}^{n_c} \sum_{k} \epsilon_{k\mu}\, c^{\dagger}_{k\mu} c_{k\mu} \tag{2.2}$$

where $\mu = 1, \cdots, n_c$ labels different electronic flavors like different bath reservoirs or different spins (e.g. for one spinful reservoir $\mu = \uparrow, \downarrow$). The operator $c^{(\dagger)}_{k\mu}$ annihilates (creates) an electron of type μ with energy $\epsilon_{k,\mu}$. The energy support of the electronic bath is defined by the bandwidth of the given problem. For a standard NRG calculation, all energies lie in the interval $[-D, D]$, where D is the non-interacting half-bandwidth and the Fermi energy is situated in the middle of the interval, $\epsilon_F \equiv 0$, assuming the same band structure for all electronic species. Henceforth, we stick to the usual NRG convention which takes $D = 1$ as energy unit.

To illustrate how the method works we discuss the simplest case, the single impurity Anderson model (SIAM), where a single spinful impurity level is coupled to an electronic reservoir (Sec. 1.4)

$$H_{imp} = \sum_{\sigma} \epsilon_d\, d^{\dagger}_{\sigma} d_{\sigma} + U n_{\uparrow} n_{\downarrow} \tag{2.3}$$

$$H_{bath} = \sum_{k\sigma} \epsilon_k\, c^{\dagger}_{k\sigma} c_{k\sigma} \tag{2.4}$$

$$H_{hyb} = \sum_{k\sigma} V_k \left(c^{\dagger}_{k\sigma} d_{\sigma} + d^{\dagger}_{\sigma} c_{k\sigma} \right) \tag{2.5}$$

with $\sigma = \uparrow, \downarrow$, replacing μ. The annihilation (creation) operators for the bath are represented as usual by $c_{k\sigma}^{(\dagger)}$. The influence of the bath onto the impurity is fully encoded in the spectral part of the hybridization function $\Gamma(\omega) = \pi \sum_k V_k^2 \, \delta(\omega - \epsilon_k)$. The central idea is that any reformulation of the Hamiltonian leaving $\Gamma(\omega)$ invariant will give the same physics. Taking a constant hybridization [13] one can rewrite the Hamiltonian in a one-dimensional energy representation

$$H = H_{imp} + \sum_\sigma \int_{-1}^{1} d\epsilon \, \epsilon \, a_{\epsilon\sigma}^\dagger a_{\epsilon\sigma} + \sum_\sigma \int_{-1}^{1} d\epsilon \sqrt{\frac{\Gamma(\epsilon)}{\pi}} \big(d_\sigma^\dagger a_{\epsilon\sigma} + h.c. \big) \tag{2.6}$$

where the continuum fermionic operators $a_{\epsilon\sigma}^{(\dagger)}$ are defined by

$$a_{\epsilon\sigma}^{(\dagger)} = \frac{c_{k\sigma}^{(\dagger)}}{\sqrt{\rho_0(\epsilon)}}, \tag{2.7}$$

$\rho_0(\epsilon)$ being the non-interacting density of states. For the continuum operators the anti-commutation relation $\{a_{\epsilon\sigma}, a_{\epsilon'\sigma'}^\dagger\} = \delta(\epsilon - \epsilon')\delta_{\sigma,\sigma'}$ holds, so that only the combination in the Eq. (2.7) is dimensionless. The energy representation of the hybridization function is

$$\Gamma(\epsilon) = \pi V^2 \rho_0(\epsilon) \, . \tag{2.8}$$

Next we discretize the energy formulation of the Hamiltonian, Eq. (2.6).

2.1 Logarithmic discretization

For a numerical approach we need to discretize the energy band. To this end, Wilson introduced a logarithmic discretization [59] via a discretization parameter $\Lambda > 1$, defining intervals as

$$\pm \, [\Lambda^{-n}, \Lambda^{-(n+1)}) \qquad n = 0, 1, 2, \dots \quad , \tag{2.9}$$

with width $d_n = \Lambda^{-n}(1 - \Lambda^{-1})$. Within these intervals we now introduce a complete set of orthonormal functions $\psi_{np}^{\pm}(\epsilon)$ (see [38] for details) labeled by the integer p and we Fourier expand the operators $a_{\epsilon\sigma}^{(\dagger)}$ in this basis,

$$a_{\epsilon\sigma} = \sum_{np} \Big(a_{np\sigma} \, \psi_{np}^{+}(\epsilon) + b_{np\sigma} \, \psi_{np}^{+}(\epsilon) \Big) \tag{2.10}$$

where $a_{np\sigma}^{(\dagger)}$ and $b_{np\sigma}^{(\dagger)}$ fulfill the canonical fermionic commutation relations.
With a constant hybridization (as in the original Wilson's argument [59]) the transformed hybridization part contains only the $p = 0$ components, i.e. the impurity couples only to the $p = 0$ components of the conduction band states,

$$\sum_\sigma \int_{-1}^{1} d\epsilon \sqrt{\frac{\Gamma(\epsilon)}{\pi}} \big(d_\sigma^\dagger a_{\epsilon\sigma} + h.c. \big) = \sum_\sigma \Big(d^\dagger \sum_n (\gamma_n^+ \, a_{n0\sigma} + \gamma_n^- \, b_{n0\sigma}) + h.c. \Big) \tag{2.11}$$

where $\gamma_n^\pm$ represents a proper normalization in the corresponding interval, derived from $\Gamma(\epsilon)$. Turning to the conduction electron term we make the approximation of dropping the $p \neq 0$ states. This is motivated by the fact that these states are coupled to the impurity only indirectly via the $p = 0$ states and that this coupling is small compared

to the couplings between the impurity and the $p = 0$ states. One can then view the couplings to the $p \neq 0$ states as small parameters, neglected in 0th order [59]. Therefore the bath Hamiltonian is approximated by a single state per interval.
Finally, after dropping the $p = 0$ terms, relabelling $a_{n0\sigma} \equiv a_{n\sigma}$ and $b_{n0\sigma} \equiv b_{n\sigma}$, we arrive at the discretized Hamiltonian

$$H = H_{imp} + \sum_{n\sigma} \left(\xi_n^+ a_{n\sigma}^\dagger a_{n\sigma} + \xi_n^- b_{n\sigma}^\dagger b_{n\sigma}\right) + \sum_\sigma \left(d_\sigma^\dagger \sum_n (\gamma_n^+ \, a_{n\sigma} + \gamma_n^- \, b_{n\sigma}) + h.c.\right) \quad (2.12)$$

where $\xi_n^\pm$ are the representative energies in the corresponding intervals, derived as well from $\Gamma(\epsilon)$. However, the coarse graining yields to misrepresenting the effective hybridization of the bath and to artificial oscillations for the calculation of physical quantities. As it is not possible, in the actual calculations, to retrieve the continuum by taking the limit $\Lambda \to 1$ or by also taking into account the $p \neq 0$ states, a procedure of averaging over various discretization grids for fixed Λ has been suggested [30]. One introduces a parameter z, uniformly distributed in $(0, 1]$, shifting the discretization points x_n like

$$\begin{aligned} x_1^z &= 1 \\ x_n^z &= \Lambda^{2-n-z} \qquad n = 2, 3, \ldots \, . \end{aligned} \quad (2.13)$$

Although the z-averaging cannot replace the continuum limit $\Lambda \to 1$ by considering infinite "z-shifts", averaging over various grids generated in this way, removes certain artificial oscillations.
Finally, since we consider NRG within DMFT, we note that we only need to calculate the self-energy and use the so-called "self-energy trick" [37], which allows to compute the self-energy via the ratio of a two-particle and a one-particle retarted Green functions, further reducing artificial oscillations. We also note that, within DMFT, the hybridization function can have an arbitrary shape and so the discretization scheme becomes essential for the accuracy of the NRG calculations. In this thesis, we use an adaptive logarithmic grid developed by R. Žitko [62], which takes the shape of the hybridization function into account and reproduces the exact input hybridization function after z-averaging.

2.2 Wilson chain

The next step in the NRG procedure is the mapping of the discrete Hamitonian onto a semi-infinite tight-binding chain, the so-called "Wilson chain". In the Hamiltonian for the Wilson chain, the impurity directly couples only to one conduction band state with operators $f_{0\sigma}^{(\dagger)}$, whose form can be read off from the hybridization terms of Eq. (2.12),

$$f_{0\sigma} = \frac{1}{\sqrt{\xi_0}} \sum_n (\gamma_n^+ \, a_{n\sigma} + \gamma_n^- \, b_{n\sigma}) \quad (2.14)$$

in which the normalization constant is given by

$$\xi_0 = \sum_n \left((\gamma_n^+)^2 + (\gamma_n^-)^2\right). \quad (2.15)$$

We then construct a new set of mutually orthogonal operators $f_{n\sigma}^{(\dagger)}$ from $f_{0\sigma}^{(\dagger)}$ and $a_{n\sigma}^{(\dagger)}$,$b_{n\sigma}^{(\dagger)}$ by a standard tridiagonalization procedure (e.g. Lanczos algorithm) to obtain the desired

chain Hamiltonian

$$H_{chain} = H_{imp} + \sqrt{\frac{\xi_0}{\pi}} \sum_{\sigma} \left[d_\sigma^\dagger f_{0\sigma} + h.c. \right] + \sum_{\sigma,n=0}^{\infty} \left[\epsilon_n f_{n\sigma}^\dagger f_{n\sigma} + t_n \left(f_{n\sigma}^\dagger f_{n+1\sigma} + h.c \right) \right], \quad (2.16)$$

with the operators $f_{n\sigma}^{(\dagger)}$ corresponding to the n-th site of the conduction electron part of the chain. The parameters of the chain are the on-site energies ϵ_n and the hopping matrix elements t_n. For a particle-hole symmetric hybridization function, $\Gamma(\omega) = \Gamma(-\omega)$, the on-site energies are zero, $\epsilon_n = 0$, for all n.
The operators $f_{n\sigma}^{(\dagger)}$ are related to the operators $a_{n\sigma}^{(\dagger)}$,$b_{n\sigma}^{(\dagger)}$ via an orthogonal trasformation, whose coefficients as well as the parameters ϵ_n, t_n can be derived via recursion relations (for details see [38]). To summarize, we obtain a chain Hamiltonian where the first site represents the impurity, which is coupled to the first site of the conduction band. All other sites of the chain represent the bath and couple to their next neighbors via the hoppings t_n.

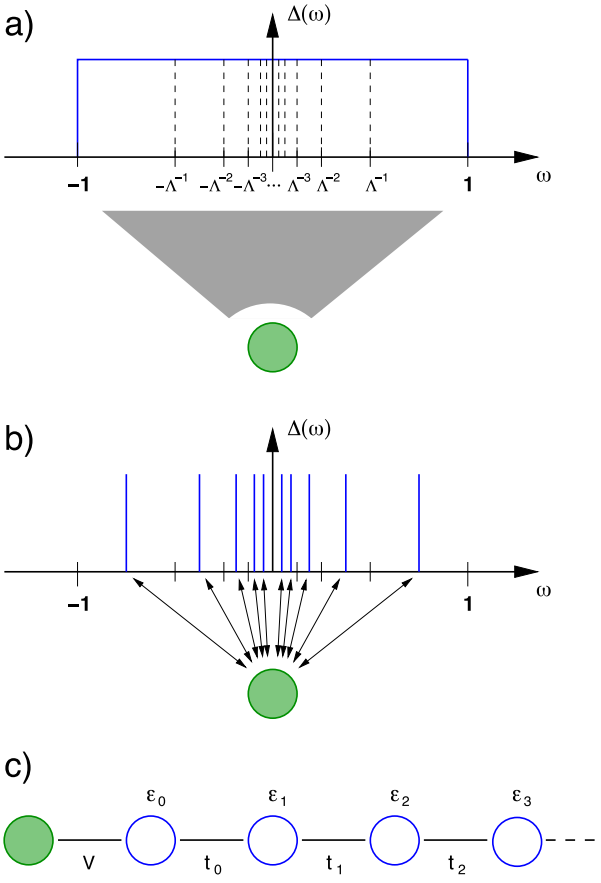

Figure 2.1: Illustration of NRG steps for SIAM where an impurity (filled circle) couples to a continuous conduction band via a constant hybridization function; a) the logarithmic discretization of the band; b) the continuous spectrum is approximated by a single state in each interval; c) the discrete Hamiltonian is mapped onto a semi-infinite tight-binding chain where the impurity (first site) couples to the first electron site via the hybridization V; the ϵ_n are the on-site energies and t_n the hopping matrix elements. Figure from [38].

Constant hybridization function

Originally Wilson [59] derived an analytical expressions for the parameters t_n in the case of a constant hybridization function $\Gamma(\omega) \equiv \Gamma = \pi V^2 \rho_0$.
We then have $\epsilon_n = 0$ for all n and the expression for the t_n reads

$$t_n = \left(\frac{(1+\Lambda^{-1})(1-\Lambda^{-n-1})}{2\sqrt{1-\Lambda^{-2n-1}}\sqrt{1-\Lambda^{-2n-3}}} \right) \Lambda^{-\frac{n}{2}} \quad \overset{n\gg 1}{\longrightarrow} \quad \left(\frac{1+\Lambda^{-1}}{2} \right) \Lambda^{-\frac{n}{2}} \tag{2.17}$$

For non-constant hybridization function $\Gamma(\omega)$, the hoppings t_n are numerically determined. However, due to the logarithmic discretization, the matrix elements fall off exponentially for large n in the general case too,

$$t_n \overset{n\gg 1}{\longrightarrow} \Lambda^{-\frac{n}{2}} \,. \tag{2.18}$$

This behavior follows directly from the logarithmic coarse graining and is of major conceptual importance for the whole method to work. The NRG mapping procedure for a constant hybridization function is depicted in Fig. 2.1.

2.3 Iterative diagonalization

The form of the chain Hamiltonian (Eq. (2.16)) allows to define an iterative renormalization group (RG) procedure. We can in fact view the chain Hamiltonian Eq. (2.16) as a series of Hamiltonians H_N ($N = 0, 1, 2, \dots$) which approaches the original Hamiltonian in the $N \to \infty$ limit

$$H = \lim_{N\to\infty} \Lambda^{-\frac{(N-1)}{2}} H_N \tag{2.19}$$

with

$$H_N = \Lambda^{\frac{(N-1)}{2}} \left(H_{imp} + \sqrt{\frac{\xi_0}{\pi}} \sum_\sigma \left(d_\sigma^\dagger f_{0\sigma} + h.c. \right) + \sum_{\sigma,n=0}^{N} \epsilon_n f_{n\sigma}^\dagger f_{n\sigma} + \sum_{\sigma,n=0}^{N-1} t_n \left(f_{n\sigma}^\dagger f_{n+1\sigma} + h.c \right) \right) \tag{2.20}$$

where the factor $\Lambda^{\frac{(N-1)}{2}}$ cancels the N dependence of t_{N-1}, the hopping matrix element between the last two sites of H_N. Such a scaling is useful for the discussion of fixed points. In fact the iterative RG procedure presented in this section is also used to study the renormalization group flow of the lowest energy levels, by which one can analyze the the behavior of the impurity model at different energy scales [13].
The recursion relation between two successive Hamiltonians is

$$H_{N+1} = \sqrt{\Lambda}\, H_N + \Lambda^{N/2} \sum_\sigma \epsilon_{N+1} f_{N+1\sigma}^\dagger f_{N+1\sigma} + \Lambda^{N/2} \sum_\sigma t_N \left(f_{N\sigma}^\dagger f_{N+1\sigma} + h.c \right) \tag{2.21}$$

and the starting point is

$$H_0 = \Lambda^{-\frac{1}{2}} \left(H_{imp} + \sum_\sigma \epsilon_0 f_{0\sigma}^\dagger f_{0\sigma} + \sqrt{\frac{\xi_0}{\pi}} \sum_\sigma \left(f_{0\sigma}^\dagger f_{0\sigma} + h.c. \right) \right). \tag{2.22}$$

This Hamiltonian corresponds to a two-site cluster formed by the impurity and the first conduction electron site. The recursion relation Eq. (2.21) can be interpreted as a renormalization group transformation R,

$$H_{N+1} = R(H_N) \tag{2.23}$$

In a standard RG transformation, the Hamiltonians are specified by a set of parameters $\vec{K}$ and the mapping R transforms the Hamiltonian $H(\vec{K})$ into another Hamiltonian of the same form $H(\vec{K'})$ with a new set of parameters $\vec{K'}$. For the H_N obtained in the NRG iterations, a representation in which the Hamiltonian can be specified by a fixed set of parameters $\vec{K}$ does not exist however. Instead we characterize H_N directly by the many-particle energies $E_N(r)$,

$$H_N \left|r\right\rangle_N = E_N(r) \left|r\right\rangle_N \qquad r = 1, \ldots, N_s \tag{2.24}$$

with the eigenstates $\left|r\right\rangle_N$ and N_s the dimension of H_N.
We can then set up an iterative procedure from site N to site $N+1$ as follows:

- We assume we have already diagonalized H_N as $H_N \left|r\right\rangle_N = E_N(r) \left|r\right\rangle_N$ with eigenenergies $E_N(r)$ and eigenstates $\left|r\right\rangle_N$. We set the ground state energy to zero and we rescale the energies $E_N(r)$, initially with level spacing of order 1, by $\Lambda^{\frac{1}{2}}$.

- We add the new Wilson site with basis states $\left|\sigma\right\rangle_{N+1}$ of dimension d, which acts as a perturbation of order $1/\sqrt{\Lambda}$. The added site therefore lifts the degenarcy of the eigenenergies $E_N(r)$ and leads to an enlarged basis set $\left|r,\sigma\right\rangle_{N+1} = \left|\sigma\right\rangle_{N+1} \otimes \left|r\right\rangle_N$ corresponding to a growth of the Hilber space by a factor d. The new Hamiltonian H_{N+1} is then diagonalized, yielding the new eigenenergies $E_{N+1}(r)$ and eigenstates $\left|r\right\rangle_{N+1}$. Finally, we set the ground state energy to zero, for convenience.

- Since the Hilbert space grows exponentially with the number of sites of the Wilson chain, it is not feasible to keep all the eigenstates and eigenenergies during the iterative procedure. Instead we truncate the state space, keeping only the N_k lowest lying eigenstates so that the dimension of the Hilbert space is kept constant and the computation time increases linearly with the length of the chain. As said, adding a new site can be seen as a perturbation of order $1/\sqrt{\Lambda}$. Hence, for sufficiently large Λ (tipically $\Lambda > 2$), the truncation scheme can be motivated arguing that the influence of high-energy states on the low-energy spectrum is small if the perturbation is weak compared to the energy of high lying states. We note that *a priori* there is no prescription for the number of states N_k one should keep. There is, however, a quantitative criterion, the so-called discarded weight, to analyze the convergence for a given NRG calculation, which can be determined from the same NRG run [55].

- We stop the iterative producedure at the site N_{max}, chosen such that all relevant physics of the actual model is captured by the resolution of the NRG calculation. At this last site all states are discarded. To summarize, the steps of the iterative RG procedure are illustrated in Fig. 2.2.

We stop the iterative producedure at the site N_{max}, determined as the required energy resolution for the given physical problem.

Finally, we note that, in the iterative procedure, the new eigenstates $\left|r'\right\rangle_{N+1}$ are related to the old eigenstates $\left|r\right\rangle_N$ via an unitary trasformation $A^{[N]}$

$$\left|r'\right\rangle_{N+1} = \sum_{\sigma_N\, r} \left[A^{[\sigma_N]}\right]_{rr'} \left|\sigma_N\right\rangle \left|r\right\rangle_N \ . \tag{2.25}$$

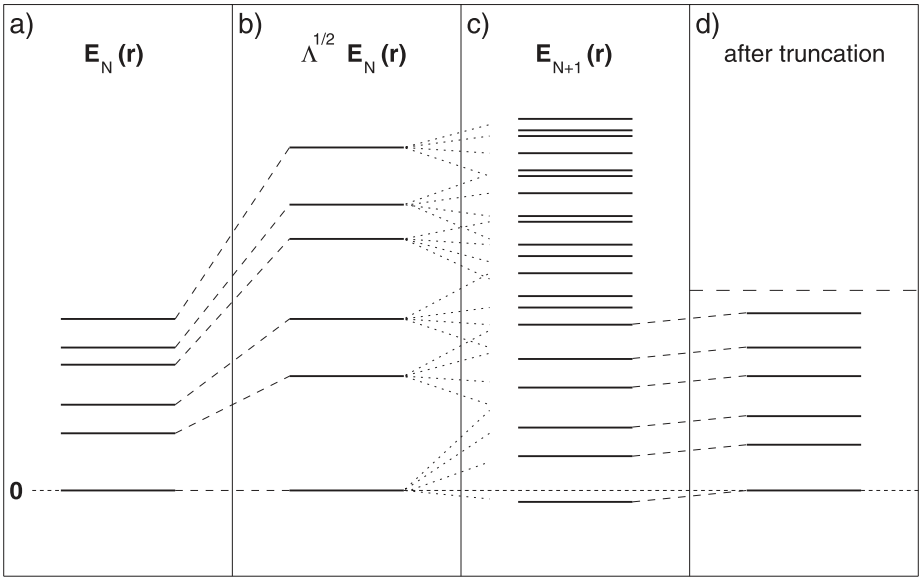

Figure 2.2: Iterative NRG procedure. a) Energy spectrum $E_N(r)$ of Hamiltonian H_N. b) Rescaling of eigenenergies by $\Lambda^{1/2}$. c) Diagonalization of the new Hamiltonian H_{N+1} with eigenenergies $E_{N+1}(r)$. d) truncation where only the N_k lowest lying states are kept and the ground state energy is set to zero. Figure from [38]

$A^{[N]}$ stands for all the d matrices $\left[A^{[\sigma_N]}\right]_{rr'} = \left(\langle r|_N \langle \sigma_N| \right) |r'\rangle_{N+1}$. This formulation of the unitary transformation has the structure of Matrix Product States (MPS) and, in fact, it turns out that an implementation of the whole NRG procedure in terms of MPS is possible and quite powerful [56]. The code in our group relies on the library QSpace [57], a tensor network library which allows to efficiently exploit both Abelian and Non-Abelian symmetries within a unified tensor representation for quantum symmetry spaces. Therefore, for a given model the maximum number of symmetries can be exploited which, in turn, results in a tremendous gain in numerical efficiency.

Many-body basis and calculation of physical quantities

At each step of the NRG calculations we perform a truncation of the Hilbert space by retaining only a certain number of states. The resulting eigenstates clearly do not span the whole Hilbert space. It turns out however that it is possible to construct a complete set of approximate eigenstates of the full Hamiltonian out of the discarded states [4]. From this many-body basis we can construct the full density matrix (fdmNRG) and compute real-frequency dynamical response functions through their spectral representations [58]. The resolution of dynamical correlation functions at finite frequencies can be further improved via a scheme of adaptive broadening for the discrete data of the NRG run [42]. By analyzing the sensitivity of discrete data to z-shifts we can deduce whether some features are physical or due to numerical artifacts. In particular the resolution enhancement is more significant for multiband calculations as we perform in this thesis.

2.3.1 Interleaved NRG

The main drawback of NRG is the poor scaling in multiband models. When we deal with m distinct flavors we have m Wilson chains, which leads to an exponential growth of the computational cost. In fact at each step of the NRG run we need to diagonalize a Hilbert

space of size $N_{tot} = N_k \times d_{loc}$. Here N_k is the number of kept states which, for converged NRG calculations, scales exponentially with the number of flavors, $N_k \equiv N_k^{(m)}$ [23]. On the other hand the dimension of the newly added site d_{loc} also scales exponentially with m. The final result reads

$$N_{tot} = N_k^{(m)} \times d_f^m \tag{2.26}$$

where d_f is the state space dimension of a single flavor. In pratice, this scaling imposes severe limitations on the applicability of NRG to multiband systems.
However a different startegy which takes use of a modified discretization has been proposed [3]. This "interleaved" NRG (iNRG) method introduces slightly different discretization schemes for the conduction bands of m different electronic flavors such that we obtain m inequivalent Wilson chains, which are interleaved to form a single generalized Wilson chain (m times longer than the standard Wilson chain, Fig. 2.3). It is important to point out that this inteleaved chain still has the exponential energy-scale separation property. Instead of performing the diagonalization for the entire "shell" of m flavors, in iNRG the diagonalization and truncation step is done separately after the addition of each electron flavor. This leads to a reduction of the local space from $d_{loc} = d_f^m$ to $d_{loc}^{iNRG} = d_f$, which in turn dramatically reduces numerical costs [23]. However we note that iNRG artificially introduces energy-scale separation between flavors connected by symmetries in the bare model and hence weakly breaks SU(N) channel symmetry, if present. Nevertheless, iNRG is comparable to standard NRG for high-symmetry models and, more importantly, it is a viable option to study low-symmetry models, inaccessible to standard NRG.

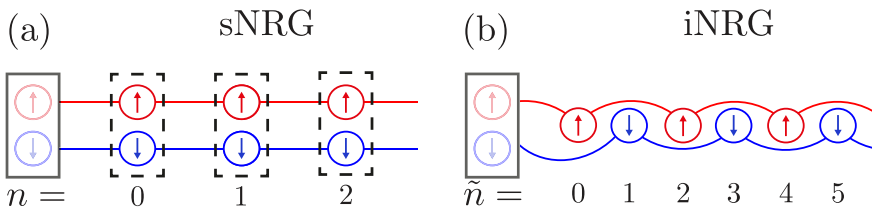

Figure 2.3: Illustration for a spinful single-band model, $m = 2$. (a) Standard Wilson chain (sNRG). (b) Interleaved Wilson chain (iNRG). In sNRG, subsites for spin-up (red) and spin-down (blue) form supersites n (dashed boxes). In iNRG the subsites are interleaved in linear fashion and labelled by $\tilde{n}$. Figure from [23].

Chapter 3

Three-band model and Spin-Orbit coupling

A large class of materials with partially filled d-shells are characterized by strong correlations, for which single-particle descriptions fail to describe, even qualitatively, their physical properties due to the strong interactions between electrons. Among these materials, the physics of early transition metal oxides (TMOs) can be captured by a three-band model, which is adopted in this thesis. To see why we can describe these d-orbital compounds (the d orbitals are actually five) with a model with just three orbitals, let's look at how the atomic orbital structure changes when an isolated atom is embedded in a solid. Let us recall that the atomic d-shell for an isolated atom consists of five orbitals, as Fig. 3.1 illustrates.

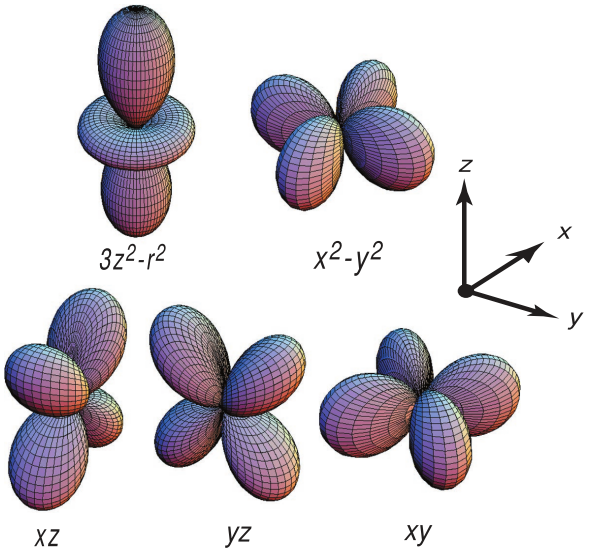

Figure 3.1: Illustration of the five d orbitals: $3z^2 - r^2$, $x^2 - y^2$, xz, yz and xy. Note that the former two orbitals are aligned along the coordinates axes, while the latter three are not. Figure from [51].

These five orbitals are formed by linear combinations of the spherical harmonics Y_l^m, with orbital angular momentum $l = 2$ and magnetic quantum number $m = -l, \ldots, l$,

namely

$$
\begin{aligned}
d_{3z^2-r^2} &= Y_2^0 \\
d_{x^2-y^2} &= \frac{1}{\sqrt{2}}\left(Y_2^2 + Y_2^{-2}\right) \\
d_{xz} &= -\frac{1}{i\sqrt{2}}\left(Y_2^1 - Y_2^{-1}\right) \\
d_{yz} &= -\frac{1}{i\sqrt{2}}\left(Y_2^1 + Y_2^{-1}\right) \\
d_{xy} &= \frac{1}{i\sqrt{2}}\left(Y_2^2 - Y_2^{-2}\right)
\end{aligned}
\tag{3.1}
$$

In free space, a transition metal ion has full rotational symmetry $SO(3)$ and the five orbital are degenerate, but when placed in a crystal the degeneracy is partly lifted due to the crystal environment [43]. Frequently, metallic ions in crystals are embedded in a regular octahedral cage, surrounded by ligands (oxygen for TMOs). The full rotation symmetry is then reduced to the symmetry group of the octahedron, $SO(3) \to O_h$, which consists of all the rotations which take the octahedron into itself. The five-fold degeneracy is lifted into a higher-lying two-fold degenerate e_g and a lower-lying three-fold degenerate t_{2g} manifolds, with an energy difference Δ, called crystal field splitting, see left Fig. 3.2a.

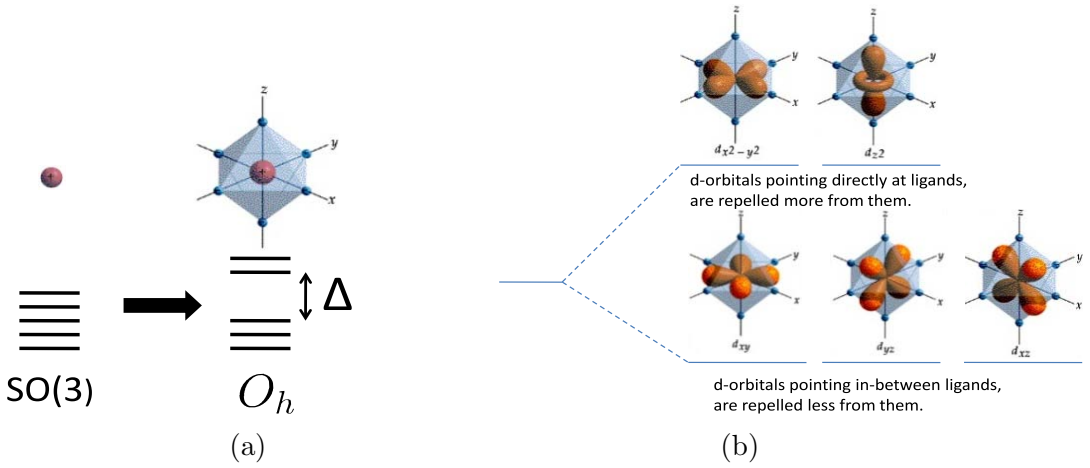

(a) (b)

Figure 3.2: In figure (a), the cubic crystal environment lowers the symmetry of the system from full $SO(3)$ to octahedral symmetry O_h and splits the d-levels into a lower-lying triply degenerate t_{2g} and higher-lying doubly degenerate e_g manifolds, with an energy difference Δ, called crystal field splitting. In figure (b), the charge distributions of d-orbitals in an octahedral cage and the ensuing splitting in e_g and t_{2g} states. Figures from [50].

If one approximates the oxigen's ligands as point charges lying on the corners of the octahedral cage, it is seen that the t_{2g} d charge distributions point in between the oxygens at the corners while the e_g orbitals (levels) point toward them. The latter therefore are more repelled and their energy is higher than the t_{2g} levels, Fig. 3.2b. The labels t_{2g} and e_g are terms from molecular symmetry theory, refering to symmetry classes to which the d-orbitals belong in octahedral complexes. In particular, the t stands for triply degenerate, while the e for doubly degenerate. The number 2 in t_{2g} represents a certain symmetry species and the subscript g indicates that the orbitals wavefunctions do not change sign under inversion about the centre of symmetry (from the German *gerade*, which means 'even').

For early TMOs (e.g. molybdates, cromates, ruthenates) with filling up to six electrons, the relevant levels are the t_{2g} orbitals. Thus a three-band model can be introduced [2]. Since the d-orbitals are well-localized and the Coulomb potential heavily screened, the t_{2g} physics can be described by a Hubbard-Kanamori Hamiltonian [20].

3.1 Three-band model

The Hubbard-Kanamori atomic Hamiltonian [20] for the t_{2g} states reads (skipping hats for operators and $\hbar = k_B = 1$ throughout)

$$\begin{aligned} H_K = U \sum_m n_{m\uparrow} n_{m\downarrow} + U' \sum_{m \neq m'} n_{m\uparrow} n_{m\downarrow} + (U' - J) \sum_{m<m',\sigma} n_{m\sigma} n_{m'\sigma} + \\ - J \sum_{m \neq m'} d^\dagger_{m\uparrow} d_{m\downarrow} d^\dagger_{m'\downarrow} d_{m'\uparrow} + J \sum_{m \neq m'} d^\dagger_{m\uparrow} d^\dagger_{m\downarrow} d_{m'\downarrow} d_{m'\uparrow} \,, \end{aligned} \tag{3.2}$$

where $d^\dagger_{m\sigma}$ creates an electron in orbital $m \in \{xz, yz, xy\}$ with spin $\sigma \in \{\uparrow, \downarrow\}$ and $n_{m\sigma}$ is the number operator.
The first three terms are density-density interactions. The first one (U) describes the interaction between electrons with opposite spins in the same orbital, the second ($U' < U$) describes opposite spins in different orbitals and the third ($U' - J$) the interaction between electrons with parallel spins in different orbitals. The latter coupling ($U' - J$) is the smallest coupling, although positive, and reflects Hund's first rule as we will see later.
The last two terms represent, respectively, the flipping of spins in two different orbitals and the hopping of two electrons from one orbital to another. Since the wave functions of t_{2g} states can be chosen real-valued, the Coulomb integrals for these two terms are equal and hence described by the same coupling J.
In order to determine the symmetries of Eq. (3.2) we consider a more general Kanamori Hamiltonian [2] where all the couplings are independent,

$$\begin{aligned} H_{GK} = U \sum_m n_{m\uparrow} n_{m\downarrow} + U' \sum_{m \neq m'} n_{m\uparrow} n_{m\downarrow} + (U' - J) \sum_{m<m',\sigma} n_{m\sigma} n_{m'\sigma} + \\ - J_{SF} \sum_{m \neq m'} d^\dagger_{m\uparrow} d_{m\downarrow} d^\dagger_{m'\downarrow} d_{m'\uparrow} + J_P \sum_{m \neq m'} d^\dagger_{m\uparrow} d^\dagger_{m\downarrow} d_{m'\downarrow} d_{m'\uparrow} \,, \end{aligned} \tag{3.3}$$

where J_{SF}, J_P are, respectively, the spin-flip and the pair-hopping couplings. This generalized Hamiltonian holds for an arbitrary number of orbitals
One can express Eq. (3.3) in a convenient way in terms of the total charge, the total spin and the total orbital isospin operators

$$\begin{aligned} N &= \sum_{m\sigma} n_{m\sigma} \,, \\ \mathbf{S} &= \frac{1}{2} \sum_{m\sigma\sigma'} d^\dagger_{m\sigma} \boldsymbol{\tau}_{\sigma\sigma'} d_{m\sigma'} \,, \\ L_m &= i \sum_{m'm''\sigma} \epsilon_{mm'm''} \, d^\dagger_{m'\sigma} d_{m''\sigma} \,, \end{aligned} \tag{3.4}$$

where $\boldsymbol{\tau}$ are the Pauli matrices and $\epsilon_{mm'm''}$ the Levi-Civita symbol. Introducing these operators, Eq. (3.3) reads

$$H_{GK} = \frac{(3U'-U)N(N-1)}{4} + (U'-U)\mathbf{S}^2 + \frac{(U'-U+J)}{2}\mathbf{L}^2 + \frac{7U-7U'-4J}{4}N + \\ + (U'-U+J+J_P)\sum_{m\neq m'} d^\dagger_{m\uparrow}d^\dagger_{m\downarrow}d_{m'\downarrow}d_{m'\uparrow} + (J-J_{SP})\sum_{m\neq m'} d^\dagger_{m\uparrow}d_{m\downarrow}d^\dagger_{m'\downarrow}d_{m'\uparrow}\,, \tag{3.5}$$

where the last two terms do not commute with $\mathbf{L}$, $[H_{GK}, \mathbf{L}] \neq 0$. For the system to be rotationally invariant, so that $\mathbf{L}$ is conserved, we need to impose some conditions on the parameters. For real-valued t_{2g} states the relation $J_{SP} = J_P = J$ holds and we can achieve rotational invariance if we set

$$U' = U - 2J\,. \tag{3.6}$$

The local t_{2g} Hamiltonian is then given by

$$H^{t_{2g}}_{local} = (U-3J)\frac{N(N-1)}{2} - 2J\mathbf{S}^2 - \frac{J}{2}\mathbf{L}^2 + \frac{5}{2}JN\,. \tag{3.7}$$

In virtue of the following commutation relations $[H^{t_{2g}}_{local}, N] = [H^{t_{2g}}_{local}, \mathbf{S}] = [H^{t_{2g}}_{local}, \mathbf{L}] = 0$, the Hamiltonian $H^{t_{2g}}_{local}$ has $U(1)_{charge} \otimes SU(2)_{spin} \otimes SO(3)_{orbital}$ symmetry. The first term describes the Coulomb repulsion depending on the total charge on site. The second term implements Hund's first rule which maximizes the total spin S. The third term implements Hund's second rule which maximizes L for a given S. The last term is proportional to N and can be absorbed in the chemical potential term. In the next subsection Hund's rules will be briefly reviewed.

3.1.1 Hund's rules

In atomic physics, Hund's rules are a set of three empirical rules used to determine the electronic configuration of the ground-state for multielectron atoms. These rules simply derive from the minimization of Coulomb repulsion between electrons and can be stated as follows:

1. One should first maximize the total spin S, hence favoring the alignment of spins in different orbitals.

2. Given S, one should maximize the total orbital angular momentum L.

3. For less than half-filled subshells, one finds the ground-state configuration by selecting the multiplet with total angular momentum $J = |L - S|$, whereas for more than half-filled, $J = L + S$.

Within the ground-state multiplet we can find the electronic configuration that satisfies the first two rules by using the bus-seat rule: fill spin-up electrons in the empty orbitals in decreasing order of $m_l = l, l-1, \ldots, -l$. When all the orbitals are singly occupied, fill in the remaining spin-down electrons to create doubly occupied orbitals, following the same decreasing order of m_l. The values of S and L depend on the number

of electrons n in the open subshells,

$$\begin{aligned} n \leq 2l+1 : S &= \frac{n}{2}, \quad L = (l+1)n - \frac{n(n+1)}{2} \\ n > 2l+1 : S &= (2l+1) - \frac{n}{2}, \quad L = (l+1)(n-(2l+1)) - \frac{(n-(2l+1))(n-2l)}{2}. \end{aligned} \tag{3.8}$$

At this point depending on the filling the third rule determines the ground-state. This latter rule reflects the spin-orbit coupling, which is assumed to be a small perturbation in the formulation of Hund's rules. We will discuss it in more detail in Sec. 3.3.
Although the Hund's rules were formulated for free ions with spherically symmetric potential, they also play an important role in solid-state physics through the coupling J, as it can be seen in the t_{2g} Hamiltonian (3.7).

3.2 Hund metals

Many correlated materials have been described in relation to the Mott state [29]. From this perspective, the strong-correlated metallic states arise due to the proximity of the Mott state, which is an insulating state where the electrons are localized by the strong Coulomb repulsion and reduced bandwidth. This state is intrinsically different from the conventional band insulator where the highest occupied band is completely filled and the Pauli principle blocks any charge fluctuations. In a Mott state the electrons become localized as the interaction strength U is equal or larger than a certain critical value U_c and double occupancies cost too much energy to be realized. In proximity of the critical value U_c, one can restore charge fluctuations by doping the insulating Mott phase with charge carriers and thus generate a strongly correlated metallic state, in which the charge fluctuations are heavily reduced, yet present. On the other hand, many multiorbital materials such as molybdates, ruthenates, iron pnictides/chalcogenides show clear signatures of strong correlations, e.g low coherence scale and small quasiparticle weight, despite being far from the Mott state[2]. It turns out that in this class of correlated but itinerant systems, the correlations are driven by the Hund interaction rather than Coulomb repulsion, leading to different physical properties from doped Mott insulators. Such materials are called "Hund metals" [61]. The relation of the Hund coupling J and Mott transition is double-faced: on the one hand, for a non-half-filled shell, J reduces the effective Coulomb repulsion U, driving the system away from the Mott transition. On the other hand, J suppresses the quasiparticle coherence scale, thus reducing the quasiparticle weight Z and making the metallic states more correlated, Fig. 3.3.

Another remarkable property of Hund metals is the so-called spin-orbital separation [49], which, not being present in Mott strongly-correlated materials [7], distinguishes Mott and Hund physics. This phenomenon refers to the screenings of spin and orbital degrees of freedom and the different energy scales at which they occur, see Fig. 3.4. In fact, in presence of Hund coupling the orbital degrees of freedom are screened at much higher energies than the spin degrees of freedom, while this separation is not present in the case $J = 0$ [49]. This separation is enhanced with increasing Hund coupling and thus the crossover from the incoherent metallic state to the coherent Fermi-liquid state, which is marked by the screening of spin fluctuations, is pushed to lower energies. The incoherent regime that opens up in between the two screenings is characterized by Non-Fermi-liquid features such as fractional power laws for the imaginary parts of the self-energy and of

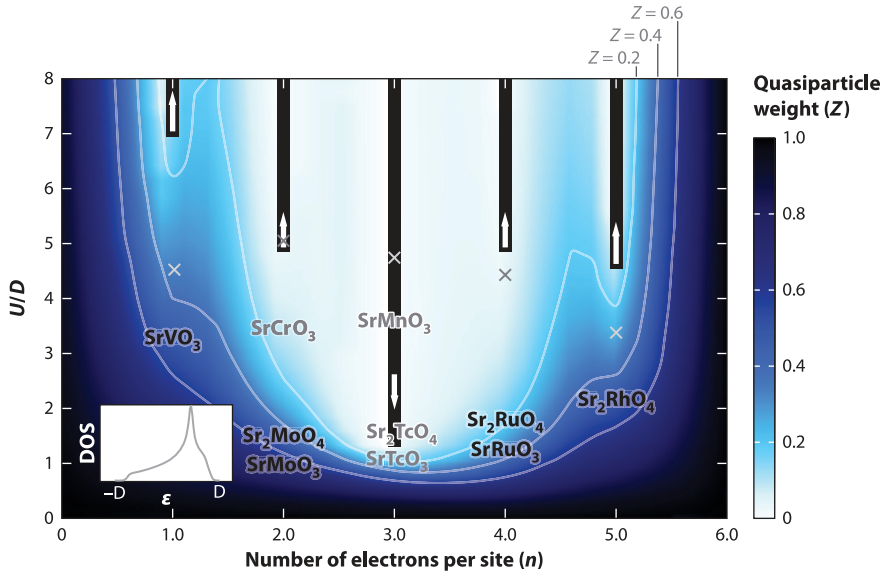

Figure 3.3: Color intensity map showing the degree of correlation for the three-band Hubbard-Kanamori model for t_{2g} orbitals. The DMFT calculations have used the realistic density of states shown on the lower left inset. The map shows the quasiparticle weight Z (color intensity) in a diagram U/D versus the filling n. The value of J is taken as $J = (0.15)U$. The grey X marks show the values of U_c in the case $J = 0$. The white arrows describe the evolution of the critica values U_c once the Hund's coupling is present. Except for half filling, J increases the critical values for the Mott transition. Some materials are also placed on the diagram as examples. Figure from [2].

susceptibilities on a real frequency axis [49, 54]. Moreover, the effects related to Hund physics are more pronounced one electron away from half-filling [10], that is two and four electrons for the three-band model. In order to analyze the effects of spin-orbit coupling on Hund physics, the focus of this thesis is on a filling of two electrons per site.

3.3 Spin-orbit coupling

The spin-orbit coupling is a relativistic correction that one obtains from the Dirac equation by considering the terms of order $\mathcal{O}(\frac{v^2}{c^2})$ [46, Chapter 9]. It is one of the so-called *fine-structure* terms, which further split the energetic spectra of atoms. Heuristically, this effect can be understood as the interaction of the spin of the electron with the magnetic field generated by the motion of the nucleus around it (in the electron rest frame). From the Lorentz force law, the magnetic field experienced by an electron is then (in CGS)

$$\mathbf{B} = -\mathbf{v} \times \frac{\mathbf{E}}{c}\,, \tag{3.9}$$

where $\mathbf{v}$ is the velocity of the nucleus in the co-moving electron frame and $\mathbf{E}$ is the electric field of the nucleus, which is generated by the central potential $\Phi(r)$ as

$$\mathbf{E} = -\frac{\mathbf{r}}{r}\frac{d\Phi(r)}{dr}\,. \tag{3.10}$$

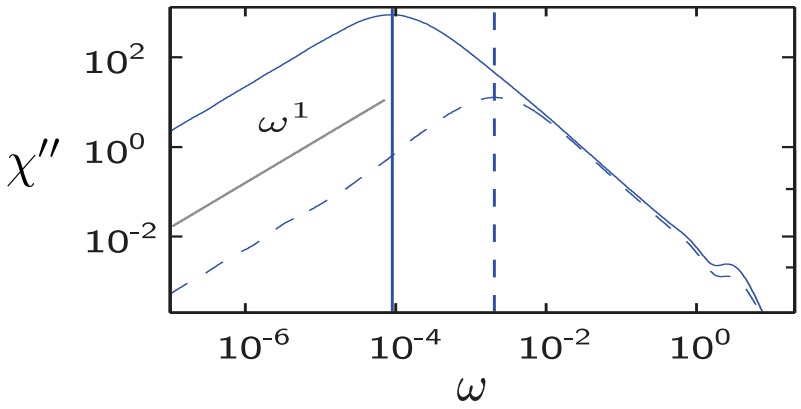

Figure 3.4: NRG calculation illustrating spin-orbital separation by plotting the imaginary parts of spin (solid line) and orbital (dashed line) susceptibilities on a real-frequency logarithmic scale. The onset of the screening process for spin and orbital degrees of freedom occur at different energy scales (marked by vertical lines). After the degrees of freedom are quenched, a Fermi-liquid linear behavior is found, $\chi'' \propto \omega$. Parameters used: $U = 6$, $J = 1$, $T = 10^{-8}$, $n_d = 2$, $\Gamma = 1$, $D = 1$. Figure from [49].

Then the interaction energy between the spin magnetic moment of the electron and the magnetic field is given by ($\hbar \equiv 1$)

$$-\boldsymbol{\mu} \cdot \mathbf{B} = g \frac{e}{2mc} \mathbf{s} \cdot \mathbf{B} \tag{3.11}$$

where $g \approx 2$ is the electron g-factor.
Using (3.9) and (3.10), the interaction energy becomes

$$\begin{aligned} -\frac{e}{mc^2} \mathbf{s} \cdot (\mathbf{v} \times \mathbf{E}) &= \frac{e}{m^2 c^2 r} \frac{d\Phi(r)}{dr} \mathbf{s} \cdot (\mathbf{p} \times \mathbf{r}) \\ &= -\frac{e}{m^2 c^2 r} \frac{d\Phi(r)}{dr} \mathbf{s} \cdot \mathbf{l} = \lambda \mathbf{l} \cdot \mathbf{s} \,. \end{aligned} \tag{3.12}$$

This result must be multiplied by a factor of $1/2$, due to the Thomas precession, since the rest frame of the electron is not inertial.
By inserting the average of the radial part $\frac{1}{r} \frac{d\Phi(r)}{dr}$, one finds that $\lambda > 0$ and $\lambda \propto Z^4$, with Z atomic number. Hence the effects of this spin-orbit coupling (SOC) become especially relevant in heavier atoms, while they are often neglected for light elements.
In a multielectronic atom the total SOC is given by the sum of the one-particle terms,

$$H_{SOC} = \lambda \sum_i \mathbf{l}_i \cdot \mathbf{s}_i \,, \tag{3.13}$$

where the index i runs over all the electrons of the open subshells.
Going back to the Hund's rules, these are formulated assuming that the part of the Coulomb interaction depending on L and S is much larger than the spin-orbit coupling. In this case, L and S are still good quantum numbers and the SOC is a small perturbation that shifts the energy levels within the (L, S) multiplet determined by the first two Hund's rules. This scheme is called *LS coupling* or *Russel-Saunders coupling*, and is well-realized in light atoms.
In order to calculate the first-order energy correction of (3.13), one averages this operator

with respect to the unperturbed states within the (L, S) multiplet to obtain the operator H_{LS}. From considerations of symmetry, it is clear that the mean values of $\mathbf{s}_i$ are directed along the total spin $\mathbf{S}$ and $\mathbf{l}_i$ along $\mathbf{L}$, so that H_{LS} has the following form

$$H_{LS} = A\,\mathbf{L}\cdot\mathbf{S}\,, \tag{3.14}$$

where A is a constant characterising the unsplit term, i.e. depending on L and S.
To determine the energy of the splitting of a degenerate state within the ground-state multiplet (L, S) the eigenvalues of the operator (3.14) are to be calculated. This can be easily done by realizing that in zero approximation the wavefunctions with definite total angular momentum J diagonalize H_{LS} and using the formula

$$\mathbf{L}\cdot\mathbf{S} = \frac{1}{2}[J(J+1) - L(L+1) - S(S+1)]\,. \tag{3.15}$$

Within the multiplet the values of L and S are the same for all the states. Therefore the value of the SOC term depends on J and the sign of A such that the energy of the multiplet splitting can be written as

$$\frac{1}{2}AJ(J+1)\,. \tag{3.16}$$

It follows that for $A > 0$ the lowest component of the multiplet has $J = |L - S|$, since it minimizes (3.16). In such case the multiplet is said to be *normal*. Whereas for $A < 0$ the lowest component has $J = L + S$. Such multiplets are called *inverted*.
It has to be determined yet whether A is positive or negative. We note that λ is positive and independent of the magnetic quantum number m_l. Therefore, if the open subshell is at most half-filled, the spins are parallel according to Hund's first rule, i.e. $\mathbf{s}_i = \mathbf{S}/n$, with n number of electrons. The SOC Hamiltonian (3.13) can then be written as

$$H_{SOC} = \lambda \sum_i \mathbf{l}_i\cdot\mathbf{s}_i = \lambda \sum_i \mathbf{l}_i\cdot\frac{\mathbf{S}}{n} \sim \frac{1}{n}\lambda\,\mathbf{L}\cdot\mathbf{S} \tag{3.17}$$

from which

$$A = \frac{\lambda}{n} = \frac{\lambda}{2S} > 0\,. \tag{3.18}$$

For a shell which is more than half-filled, we can imagine to start off with the filled shell, for which $H_{SOC} = 0$, and then add holes to obtain the original electronic configuration. So, we can write the SOC operator as $-\lambda \sum_i \mathbf{l}_i\cdot\mathbf{s}_i$ where the sum is over the holes. In this case, we have $S = -\sum_i \mathbf{s}_i$ and $L = -\sum_i \mathbf{l}_i$ and by the same argument as before it follows $A = -\lambda/2S < 0$.

We then find that for less than half-filled shells the most favorable value of J is $|L-S|$, whereas for more than half-filled shells is $L + S$. For a half-filled shell of orbitals with angular momentum l, one has $L = 0$ and $S = (2l+1)/2$, and so $|L - S| = L + S = S$. This shows that Hund's third rule originates from the SOC term. We underline that the scheme of construction of the Hund's rules is based on the assumption that L and S are good quantum numbers and given by the combination of the orbital angular momenta and the spins of the electrons, respectively. This corresponds to the case in which the SOC is much smaller than the L and S dependent part of the Coulomb energy. If it is not the case (e.g. heavier atoms) the *LS coupling* approximation can not be applied, although the classification of the lowest states based on this scheme (using L and S)

can still remain meaningful. If the SOC is larger than the L and S dependent part of the Coulomb interaction, each electron is characterized by its total angular momentum j, which are combined to give total angular momentum J, i.e. $\mathbf{J} = \sum_i \mathbf{j}_i$ (rather than $\mathbf{J} = \mathbf{L} + \mathbf{S}$ as in *LS coupling*). This scheme for arranging the atomic levels is called *jj-coupling*. Although this scheme can be used to a good approximation in heavy elements where the SOC is comparable to the Coulomb energy, in practice it is never realized in its pure form and various types of intermediate couplings between LS and jj are used to describe the atomic levels of heavy atoms.

For one electron with spin $s = 1/2$ in an orbital with angular momentum l the total angular momentum j takes on the values $j = l \pm 1/2$ and the eigenenergies of the one-particle SOC term $\lambda \mathbf{l} \cdot \mathbf{s}$ are

$$\frac{\lambda}{2}\left(j(j+1) - l(l+1) - \frac{3}{4}\right) = \lambda \begin{cases} l/2\,, & j = l + \frac{1}{2} \\ -(l+1)\,, & j = l - \frac{1}{2} \end{cases} . \tag{3.19}$$

The corresponding eigenfunctions $|j, m_j, l\rangle$ can be found by using the highest weight construction from the one-particle states $|l, m_l, m_s = \uparrow, \downarrow\rangle$ ($s = 1/2$ implied). For example, for $j = l + 1/2$ the highest weight state has $m_j = l + 1/2$ and can be constructed as $|l + 1/2, l + 1/2, l\rangle = |l, l, \uparrow\rangle$. To find the other states with the same j but different m_j we apply the lowering operator $j_- = l_- + s_-$ to the highest weight state and then normalize. Applying repeatedly the lowering operator, all the states with $j = l + 1/2$ are found. The states for $j = l + 1/2$ can be constructed imposing orthogonality to the previously found states. One can write all the states in a compact form [47][Chapter 10] as follows

$$|j = l + \frac{1}{2}, m_j, l\rangle = \sqrt{\frac{l + m_j + 1/2}{2l+1}}\ |l, m_j - \frac{1}{2}, \uparrow\rangle + \sqrt{\frac{l - m_j + 1/2}{2l+1}}\ |l, m_j + \frac{1}{2}, \downarrow\rangle\ , \tag{3.20}$$

with $m_j = l + 1/2, \ldots, -(l + 1/2)$. And, for $j = l - 1/2$,

$$|l - \frac{1}{2}, m_j, l\rangle = -\sqrt{\frac{l - m_j + 1/2}{2l+1}}\ |l, m_j - \frac{1}{2}, \uparrow\rangle + \sqrt{\frac{l + m_j + 1/2}{2l+1}}\ |l, m_j + \frac{1}{2}, \downarrow\rangle\ , \tag{3.21}$$

with $m_j = l - 1/2, \ldots, -(l - 1/2)$. So far we have seen the main aspects of the SOC physics in atoms. The question that naturally arises at this point is the following: what happens when the atom is embedded in a crystal environment?

3.3.1 SOC in d-systems

We have seen that in a typical crystal environment of TMOs the metallic ion is at the center of an octahedral cage where the ligands, i.e. oxygen atoms, produce a crystal field that splits the d-orbitals in two e_g and three t_{2g} bands. Assuming a large crystal field, for a filling less or equal to six electrons, we can describe the low-energy physics of the system considering only the three t_{2g} bands. However, the SOC couples the spin and the orbital degrees of freedom and generally mixes the e_g and t_{2g} states such that, for large enough SOC, the mixing may have non-negligible effects and the full five-band model is more appropriate.

First, let's write the matrix elements of the orbital angular momentum for a single electron

with $l = 2$ in the basis of e_g and t_{2g} states (3.1), $\{d_{yz}, d_{xz}, d_{xy}, d_{3z^2-r^2}, d_{x^2-y^2}\}$, and in the atomic p-orbitals basis $\{p_x, p_y, p_z\}$,

$$l_x = \left(\begin{array}{ccc|cc} 0 & 0 & 0 & -\sqrt{3}i & -i \\ 0 & 0 & i & 0 & 0 \\ 0 & -i & 0 & 0 & 0 \\ \hline \sqrt{3}i & 0 & 0 & 0 & 0 \\ i & 0 & 0 & 0 & 0 \end{array}\right), \qquad l_x^p = \begin{pmatrix} 0 & 0 & 0 \\ 0 & 0 & -i \\ 0 & i & 0 \end{pmatrix} \tag{3.22}$$

$$l_y = \left(\begin{array}{ccc|cc} 0 & 0 & -i & 0 & 0 \\ 0 & 0 & 0 & \sqrt{3}i & -i \\ i & 0 & 0 & 0 & 0 \\ \hline 0 & -\sqrt{3}i & 0 & 0 & 0 \\ 0 & i & 0 & 0 & 0 \end{array}\right), \qquad l_y^p = \begin{pmatrix} 0 & 0 & i \\ 0 & 0 & 0 \\ -i & 0 & 0 \end{pmatrix} \tag{3.23}$$

$$l_z = \left(\begin{array}{ccc|cc} 0 & i & 0 & 0 & 0 \\ -i & 0 & 0 & 0 & 0 \\ 0 & 0 & 0 & 0 & 2i \\ \hline 0 & 0 & 0 & 0 & 0 \\ 0 & 0 & -2i & 0 & 0 \end{array}\right), \qquad l_z^p = \begin{pmatrix} 0 & -i & 0 \\ i & 0 & 0 \\ 0 & 0 & 0 \end{pmatrix}. \tag{3.24}$$

Note that all the matrix elements in the e_g states are zero, meaning that the orbital angular momentum is completely quenched. It follows that the e_g states are not affected by the SOC. By comparing the matrix elements in the t_{2g} states with those in the p states, the following relation holds

$$\mathbf{l}_{t_{2g}} = -\mathbf{l}_p \,, \tag{3.25}$$

which means that the orbital angular momentum is partially quenched in the t_{2g} states from $l = 2$ to $l = 1$. Then we can calculate the expectation value of $\mathbf{l}^2 = l_x^2 + l_y^2 + l_z^2$, $l(l+1)$, using $l = 1$ with an extra minus sign. This correspondence is called T-P equivalence [43, Chapter 7]. When the cubic crystal splitting is large, one can neglect the off-diagonal elements connecting the e_g and t_{2g} states and the T-P equivalence can be conveniently used. The one-particle SOC operator H_λ can be diagonalized as follows

$$H_\lambda = \lambda\, \mathbf{l}_{t_{2g}} \cdot \mathbf{s} = -\lambda\, \mathbf{l}_p \cdot \mathbf{s} = -\lambda \left(\mathbf{j}_{eff}^2 - \mathbf{l}_p^2 - \mathbf{s}^2 \right), \tag{3.26}$$

where with $l = 1$ and $s = 1/2$, we have $j = 1/2$ or $j = 3/2$, with degeneracy 2 and 4, respectively. Thus the eigenvalues of the SOC operator are

$$\langle H_\lambda \rangle = \begin{cases} \lambda \,, & j = \frac{1}{2} \\ -\frac{\lambda}{2} \,, & j = \frac{3}{2} \end{cases}. \tag{3.27}$$

In the j-basis the noninteracting electronic structure consists of two degenerate $j = 1/2$ bands and four degenerate $j = 3/2$ bands, lower in energy, with a spin-orbit energy

splitting of $\frac{3}{2}\lambda$. Note that the band structure is the opposite of that one would obtain for the atomic p-orbitals, due to the T-P equivalence. With the SOC the t_{2g} states are split into the j-bands, whose eigenstates in terms of t_{2g} wavefunctions, including spin, are given by

$$|j=1/2, m_j=1/2\rangle = \frac{1}{\sqrt{3}}|d_{yz\downarrow}\rangle + \frac{i}{\sqrt{3}}|d_{xz\downarrow}\rangle + \frac{1}{\sqrt{3}}|d_{xy\uparrow}\rangle \tag{3.28}$$

$$|1/2, -1/2\rangle = \frac{1}{\sqrt{3}}|d_{yz\uparrow}\rangle - \frac{i}{\sqrt{3}}|d_{xz\uparrow}\rangle - \frac{1}{\sqrt{3}}|d_{xy\downarrow}\rangle \tag{3.29}$$

$$|3/2, 3/2\rangle = -\frac{1}{\sqrt{2}}|d_{yz\uparrow}\rangle - \frac{i}{\sqrt{2}}|d_{xz\uparrow}\rangle \tag{3.30}$$

$$|3/2, -3/2\rangle = \frac{1}{\sqrt{2}}|d_{yz\downarrow}\rangle - \frac{i}{\sqrt{2}}|d_{xz\downarrow}\rangle \tag{3.31}$$

$$|3/2, 1/2\rangle = -\frac{1}{\sqrt{6}}|d_{yz\downarrow}\rangle - \frac{i}{\sqrt{6}}|d_{xz\downarrow}\rangle + \sqrt{\frac{2}{3}}|d_{xy\uparrow}\rangle \tag{3.32}$$

$$|3/2, 1/2\rangle = \frac{1}{\sqrt{6}}|d_{yz\uparrow}\rangle - \frac{i}{\sqrt{6}}|d_{xz\uparrow}\rangle + \sqrt{\frac{2}{3}}|d_{xy\downarrow}\rangle \ , \tag{3.33}$$

where it is seen how the SOC mixes states of the cubic basis with different spin and angular momenta .

In general, these eigenfunctions diagonalize the full Hamiltonian of the one-electron states that neglects the part of the SOC operator mixing the $t_{2g}-e_g$ subspaces. If one also considers the mixing term as a small perturbation [50], it is found that the $j=3/2$ and e_g states are mixed. To the first order the wavefunctions of $j=3/2$ states are modified as

$$|3/2, \pm 3/2\rangle \pm i\sqrt{\frac{3}{2}}\frac{\lambda}{\lambda/2+\Delta}|d_{3z^2-r^2}, \mp 1/2\rangle \tag{3.34}$$

$$|3/2, \pm 1/2\rangle \pm i\sqrt{\frac{3}{2}}\frac{\lambda}{\lambda/2+\Delta}|d_{x^2-y^2}, \pm 1/2\rangle \ , \tag{3.35}$$

with a second-order energy shift of $-\frac{3}{2}\frac{\lambda^2}{\lambda/2+\Delta}$. The Δ is the crystal field splitting between t_{2g} and e_g levels.
The e_g states are modified as

$$|d_{3z^2-r^2}, \mp 1/2\rangle \pm i\sqrt{\frac{3}{2}}\frac{\lambda}{\lambda/2+\Delta}|3/2, \pm 3/2\rangle \tag{3.36}$$

$$|d_{x^2-y^2}, \pm 1/2\rangle \pm i\sqrt{\frac{3}{2}}\frac{\lambda}{\lambda/2+\Delta}|3/2, \pm 1/2\rangle \ , \tag{3.37}$$

with a second-order energy shift of $+\frac{3}{2}\frac{\lambda^2}{\lambda/2+\Delta}$. Therefore we need to be careful in applying results from the three-band model to real materials. For example, typical values for $5d$ systems are $\lambda = 0.5eV$ and $\Delta = 3eV$ and the mixing is $\sqrt{\frac{3}{2}}\frac{\lambda}{\lambda/2+\Delta} \approx 0.19$, a 20% effect.

However, assuming a crystal field large enough with respect to the SOC, we can conveniently use the three-band model and the T-P equivalence. In the cubic t_{2g} basis,

the second quantized SOC Hamiltonian reads

$$H_{SOC} = -\lambda \sum_{\substack{mm' \\ \sigma\sigma'}} \langle m|\mathbf{l}_p|m'\rangle \cdot \langle \sigma|\mathbf{s}|\sigma'\rangle \, c^\dagger_{m\sigma} c_{m'\sigma'} \tag{3.38}$$

$$= \frac{i\lambda}{2} \sum_{\substack{mm'm'' \\ \sigma\sigma'}} \epsilon_{mm'm''} \, \tau^{m''}_{\sigma\sigma'} \, c^\dagger_{m\sigma} c_{m'\sigma'} \,, \tag{3.39}$$

where $c^\dagger_{m\sigma}$ creates an electron of spin $\sigma \in \{\uparrow\downarrow\}$ in the orbital $m \in \{xy, xz, yz\}$, $\tau^{m''}_{\sigma\sigma'}$ are the matrix elements of the Pauli matrices and the matrix elements of the components of $\mathbf{l}_p$ are given by $\langle m|\mathbf{l}^k_p|m'\rangle = -i\epsilon_{kmm'}$. Note that the H_{SOC} is totally off-diagonal in the cubic t_{2g} basis. We can also split the SOC operator as $H_{SOC} = H^z_{SOC} + H^{xy}_{SOC}$,

$$H^z_{SOC} = \frac{\lambda}{2} \sum_{m=-l}^{l} m \, (d^\dagger_{m\uparrow} d_{m\uparrow} - d^\dagger_{m\downarrow} d_{m\downarrow}) \tag{3.40}$$

$$H^{xy}_{SOC} = \frac{\lambda}{2} \sum_{m=-l}^{l-1} \sqrt{(l-m)(l+m+1)} \, (d^\dagger_{m+1\downarrow} d_{m\uparrow} + d^\dagger_{m\uparrow} d_{m+1\downarrow}) \,. \tag{3.41}$$

Under the particle-hole transformation, $h_{m\sigma} \to d^\dagger_{m\sigma}$ and $h^\dagger_{m\sigma} \to d_{m\sigma}$ these two components change sign, so that a site occupied by two electrons and SOC λ is equivalent to a site occupied by four electrons (two holes) and SOC $-\lambda$. Therefore the case with four electrons can be taken into account by changing the sign of λ for a filling of two electrons.

The full Hamiltonian under study can be thus written as

$$H = \sum_i \big(H_{int}\big)_i + \sum_i \big(H_{SOC}\big)_i - \mu \sum_i N_i + \sum_{\langle ij\rangle mm'\sigma} (t\delta_{mm'}) c^\dagger_{im\sigma} c_{jm'\sigma} \tag{3.42}$$

where the interacting term is

$$\big(H_{int}\big)_i = (U - 3J) \frac{N_i(N_i - 1)}{2} - 2J\mathbf{S}^2_i - \frac{J}{2}\mathbf{L}^2_i \,. \tag{3.43}$$

The index i runs over the lattice sites, μ is the chemical potential and the nearest-neighbor hopping $t\delta_{mm'}$ is taken site-independent and orbital-diagonal. The remaining operators have the usual meaning, with an extra lattice index i.
Let's determine the symmetries of the local part of the Hamiltonian,

$$H_{local} = \big(H_{int}\big)_i + \big(H_{SOC}\big)_i - \mu N_i \,. \tag{3.44}$$

Due to the SOC term, $\mathbf{L}_i$ and $\mathbf{S}_i$ are not conserved, i.e. $[H_{SOC}, \mathbf{L}_i \neq 0]$ and $[H_{SOC}, \mathbf{S}_i] \neq 0$. However, the j-basis diagonalizes the H_{SOC} and the total angular momentum $\mathbf{J} = \sum_j \mathbf{j}_j$, where $\mathbf{j}_j$ is the one-particle total angular momentum. It thus follows that $[H_{SOC}, \mathbf{J}_i] = 0$, as well as $[H_{int}, \mathbf{J}_i] = 0$. Further, H_{local} does not change the particle number. Therefore, the local Hamiltonian H_{local} has $U(1)_{charge} \otimes SU(2)_{total_J}$ symmetry, expressing the conservation of the charge and the total angular momentum.

We can rewrite the interacting Hamiltonian in the j-basis [26, 52] and split it into a pure $j_{1/2}$ part, a pure $j_{3/2}$ part and a part mixing them,

$$H_{int} = H_{j_{1/2}} + H_{j_{3/2}} + H_{mix} \tag{3.45}$$

where

$$H_{j_{1/2}} = \left(U - \frac{4}{3}J_H\right) n_{j=\frac{1}{2},m_j=\frac{1}{2}}\, n_{j=\frac{1}{2},m_j=-\frac{1}{2}} \tag{3.46}$$

$$\begin{aligned} H_{j_{3/2}} =& (U - J_H)\left(n_{\frac{3}{2},\frac{3}{2}}\, n_{\frac{3}{2},-\frac{3}{2}} + n_{\frac{3}{2},\frac{1}{2}}\, n_{\frac{3}{2},-\frac{1}{2}}\right) \\ &+ \left(U - \frac{7}{3}J_H\right)\left(n_{\frac{3}{2},-\frac{3}{2}}\, n_{\frac{3}{2},-\frac{1}{2}} + n_{\frac{3}{2},\frac{3}{2}}\, n_{\frac{3}{2},\frac{1}{2}}\right) \\ &+ \left(U - \frac{7}{3}J_H\right)\left(n_{\frac{3}{2},-\frac{3}{2}} n_{\frac{3}{2},\frac{1}{2}} + n_{\frac{3}{2},\frac{3}{2}}\, n_{\frac{3}{2},-\frac{1}{2}}\right) \\ &+ \frac{4}{3}J_H\, d^\dagger_{\frac{3}{2},-\frac{3}{2}}\, d^\dagger_{\frac{3}{2},\frac{3}{2}}\, d_{\frac{3}{2},-\frac{1}{2}}\, d_{\frac{3}{2},\frac{1}{2}} \\ &+ \frac{4}{3}J_H\, d^\dagger_{\frac{3}{2},-\frac{1}{2}}\, d^\dagger_{\frac{3}{2},\frac{1}{2}}\, d_{\frac{3}{2},-\frac{3}{2}}\, d_{\frac{3}{2},\frac{3}{2}}\,, \end{aligned} \tag{3.47}$$

and the density-density part of H_{mix} is

$$\begin{aligned} H_{mix,dd} =& \left(U - \frac{5}{3}J_H\right)\left(n_{\frac{1}{2},-\frac{1}{2}}\, n_{\frac{3}{2},\frac{3}{2}} + n_{\frac{1}{2},-\frac{1}{2}}\, n_{\frac{3}{2},-\frac{3}{2}}\right) \\ &+ (U - 2J_H)\left(n_{\frac{1}{2},\frac{1}{2}}\, n_{\frac{3}{2},\frac{1}{2}} + n_{\frac{1}{2},-\frac{1}{2}}\, n_{\frac{3}{2},-\frac{1}{2}}\right) \\ &+ \left(U - \frac{7}{3}J_H\right)\left(n_{\frac{1}{2},\frac{1}{2}}\, n_{\frac{3}{2},-\frac{1}{2}} + n_{\frac{1}{2},-\frac{1}{2}}\, n_{\frac{3}{2},\frac{1}{2}}\right) \\ &+ \left(U - \frac{8}{3}J_H\right)\left(n_{\frac{1}{2},\frac{1}{2}}\, n_{\frac{3}{2},-\frac{3}{2}} + n_{\frac{1}{2},-\frac{1}{2}}\, n_{\frac{3}{2},\frac{3}{2}}\right). \end{aligned} \tag{3.48}$$

The H_{mix} contains 30 more terms, besides the four density-density terms shown here. The operator $d^\dagger_{j,m_j}$ creates a particle with m_j in the band j. We see that $H_{j_{1/2}}$ has the form of a one-band Hubbard Hamiltonian with effective interaction $U - \frac{4}{3}J_H$. If one assigns $|m_j|$ as orbital index and the sign of m_j as the spin, the $H_{j_{3/2}}$ can be interpreted as a two-band Kanamori Hamiltonian with different prefactors. Interestingly, there is only one coupling for interorbital interactions, $U - \frac{7}{3}J_H$, instead of two, $U - 2J_H$ and $U - 3J_H$, for the Kanamori Hamiltonian in the cubic basis, see 3.2. Note that we stick to the rotationally invariant condition, $U' = U - 2J_H$, also for crystals, although it holds exacly for atomic systems only. The last two terms of $H_{j_{3/2}}$ can be interpreted as pair-hopping terms with effective strength of $\frac{4}{3}J_H$.

Chapter 4

Results

Let's set the ground for the results obtained in this thesis recalling the central points of the discussion from the previous chapters. We focus on a Hubbard-Kanamori three-band model plus spin-orbit coupling (SOC), Sec. 3.3.1, described by the following local Hamiltonian

$$H_{local} = H_{int} + H_{SOC} - \mu N \tag{4.1}$$

with

$$H_{int}\left[c^{\dagger}_{m\sigma}\right] = \left((U - 3J_H)\frac{N(N+1)}{2} - 2J_H\mathbf{S}^2 - \frac{J_H}{2}\mathbf{L}^2\right) \tag{4.2}$$

where $c^{\dagger}_{m\sigma}$ creates an electron of spin $\sigma \in \{\uparrow\downarrow\}$ in the orbital $m \in \{xy, xz, yz\}$, μ is the chemical potential, N the particle number operator, $\mathbf{S}$ the total spin operator and $\mathbf{L}$ the total orbital angular momentum operator. The SOC term in second quantization reads

$$\begin{aligned} H_{SOC} &= \lambda \sum_{mm'\sigma\sigma'} \langle m|\mathbf{l}_{t_{2g}}|m'\rangle \cdot \langle\sigma|\mathbf{s}|\sigma'\rangle \, c^{\dagger}_{m\sigma}c_{m'\sigma'} \\ &= \frac{i\lambda}{2} \sum_{\substack{mm'm'' \\ \sigma\sigma'}} \epsilon_{mm'm''} \, \tau^{m''}_{\sigma\sigma'} \, c^{\dagger}_{m\sigma}c_{m'\sigma'} \, , \end{aligned} \tag{4.3}$$

where $\tau^{m''}_{\sigma\sigma'}$ are the matrix elements of the Pauli matrices and $\epsilon_{mm'm''}$ is the Levi-Civita symbol.
Within single-site DMFT, the full lattice Hamiltonian is mapped self-consistently onto a three-band Anderson-Hund model (3AHM),

$$H = H_{int} + H_{SOC} + \epsilon_d N + \sum_{km\sigma}\left(\epsilon_k \, b^{\dagger}_{km\sigma}b_{km\sigma} + V_k\left(d^{\dagger}_{m\sigma}b_{km\sigma} + h.c.\right)\right), \tag{4.4}$$

where $d^{\dagger}_{m\sigma}$ creates an electron of spin σ in the orbital m with energy $\epsilon_d = -\mu$ at the impurity and $b^{\dagger}_{km\sigma}$ are the corresponding creation operators for the noninteracting three-band bath. The interacting part H_{int} is the same as in the local lattice Hamiltonian (4.2). The hybridization is assumed orbital-diagonal and with the same value for all the bands. Further, the three noninteracting baths are taken to have the same bandwidth $2D$. We set the half-bandwidth $D = 1$ as energy unit for all the calculations. So far we have recalled the model in the cubic t_{2g} basis, although the noninteracting part of the Hamiltonian is not diagonal due to the SOC term, which is fully non-diagonal in the cubic basis. An alternative way is to work in the j-basis that diagonalizes H_{SOC}. In this basis the noninteracting part and the hybridization function are diagonal (the $j_{1/2}$

and $j_{3/2}$ states do not mix, being separated in energy). It follows that the self-energy is diagonal as well. In case of sizable SOC this basis has to be used since L and S are not conserved (this corresponds to work in the *jj-coupling* regime). We recall that the *jj-coupling* regime corresponds to the case in which the SOC is larger compared to the part of Coulomb energy depending on L and S, which in our model is $-2J_H\mathbf{S}_i^2 - \frac{J_H}{2}\mathbf{L}_i^2$. Therefore, the SOC is to be compared with the Hund coupling J_H and for $SOC \sim J_H$ the *jj-coupling* regime can be approximately adopted. This basis is used all calculations, in which we focus on the paramagnetic phase at zero temperature $T = 0$, and analyze what effects the SOC has on the physics of the model.

4.1 NRG results

First, we perform NRG calculations without DMFT self-consistency. We use a flat hybridization function $\Gamma(\omega) = \Gamma\,\Phi(D - |\omega|)$ for all bands, with half-bandwidth $D = 1$ as energy unit, and a chemical potential μ so to obtain a filling of $\langle N\rangle = n = 2$ at the impurity. We exploit the $U(1)_{ch} \otimes SU(2)_J$ symmetry of the model, i.e. conservation of charge and total angular momentum, to reduce the numerical overhead. In all the calculations we use a discretization parameter $\Lambda = 4$ and $N_z = 2$ shifts of the discretization grid. Further, we employ an iNRG procedure (Sec. 2.3.1) for numerical efficiency, interleaving the $j = 1/2$ and $j = 3/2$ bands with 2 different permutations of the iNRG sub-channels. This interleaving scheme does not break any symmetry since the bands are already separated in energy. In the diagonalization we keep 9000 multiplets, corresponding roughly to ~ 45000 kept states. We analyze the paramagnetic phase at zero temperature ($T = 10^{-10}$) and for all the calculations we adopt the set of parameter $U/D = 3.2, J_H/D = 0.4, \Gamma \cdot D = 0.05, D = 1$, relevant to Hund physics [16].

We start analyzing the impurity spectral functions of the j-bands for positive values of λ/D, see Fig. 4.1. We first look at the Hubbard bands, emerging from incoherent atomic-like excitations. We see that the SOC has no sizable effect for the value 10^{-6}, for which the j-bands are still degenerate. As we increase the SOC to 10^{-4}, the j-bands are already clearly resolved. The spectral weight is transferred to negative energies for the $j_{3/2}$ states and to positive energies for the $j_{1/2}$ states, as the changes in the magnitudes of lower and upper Hubbard bands show. The spectral weight transfer reflects the orbital structure in the j-basis, with two degenerate $j_{1/2}$ bands and four degenerate $j_{3/2}$ bands lower in energy. As we increase the SOC, the $j_{3/2}$ states are pushed even more to negative energies, reflecting the fact that the energy difference between the bands is larger and the $j_{3/2}$ states have a higher occupancy (at $T = 0$ the occupancy is $n_j = \int_{-\infty}^{0} d\omega A(\omega)$), while the broad upper Hubbard band contains excitations to different multiplets of the half-filled impurity. On the other hand, the $j_{1/2}$ states become emptied out with increasing SOC, as we see from the low spectral weight for negative energies, while the upper Hubbard band corresponding to a $j_{1/2}$ excitation acquire a larger spectral weight.

On the other hand, with λ/D negative, see Fig. 4.2, the j-structure is inverted with the two $j_{1/2}$ bands lower in energy compared to the four $j_{3/2}$ bands. Therefore, as the SOC increases, the $j_{1/2}$ states are pushed to negative energies while the $j_{3/2}$ states to positive energies. In this scenario, for a filling of two electrons at the impurity, we approach a filled $j_{1/2}$ band with increasing SOC. In the high-energy spectrum this is seen from the large value of the spectral functions for negative energies, while the upper Hubbard band is rather flat with small spectral weight, corresponding to the fact that as the

band becomes more insulating, a particle-like excitation is blocked. Correspondingly, we observe the spectral weight of the $j_{3/2}$ states transferred to positive energies.

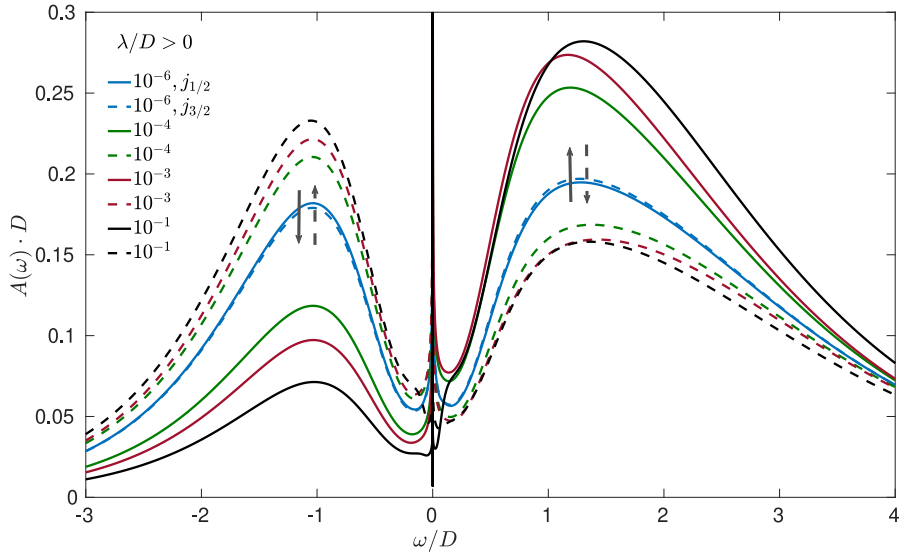

Figure 4.1: NRG spectral functions for various values of $\lambda/D > 0$. The spectral weight transfer reflects the j-basis structure with two degenerate $j_{1/2}$ bands and four degenerate $j_{3/2}$ bands, lower in energy. As λ/D increases, the spectral weights for the $j_{1/2}$ states are pushed to positive energies (as the solid grey arrows illustrate), while the $j_{3/2}$ states to negative energies (dashed grey arrows). Parameters: $n = 2, U/D = 3.2, J_H/D = 0.4, \Gamma \cdot D = 0.05, T \approx 0$.

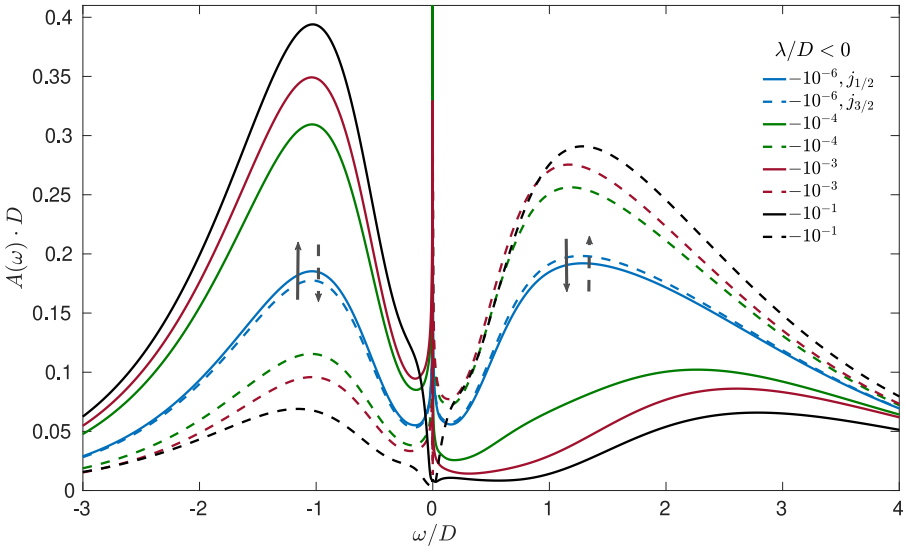

Figure 4.2: NRG spectral functions for various values of $\lambda/D < 0$. The spectral weight transfer reflects the inverted j-basis structure with four degenerate $j_{3/2}$ bands and two degenerate $j_{1/2}$ bands, which are now lower in energy . As $|\lambda|/D$ increases, the spectral weights for the $j_{1/2}$ states are pushed to negative energies (solid grey arrows), while the $j_{3/2}$ states to positive energies (dashed grey arrows). Parameters: $n = 2, U/D = 3.2, J_H/D = 0.4, \Gamma \cdot D = 0.05, T \approx 0$.

In order to analyze the low-energy spectrum we plot the close-ups of the spectral functions at the Fermi level $\omega = 0$ for both $\lambda/D > 0$ and $\lambda/D < 0$, see Figs. 4.3. For $\lambda/D > 0$ (upper panel (a)), the $j_{3/2}$ spectral functions feature coherent quasiparticle peaks at the Fermi level and thus metallic behavior. In the inset, we plot the spectral functions for $\lambda/D = 10^{-6}$ where the SOC-induced effects are not present and we observe

the characteristic asymmetric shape of the quasiparticle peak that is a fingerprint of Hund metals [49]. Remarkably, as the SOC increases, the quasiparticle peak becomes narrower, signaling a suppression of the Kondo temperature T_K (low coherence scale) and the quasiparticle weight Z (measure of how correlated the system is), since $T_K \sim Z$. The SOC thus increases the correlations. The $j_{1/2}$ spectral functions have small spectral weight at $w = 0$ with increasing SOC, reflecting the fact that the $j_{1/2}$ states have an insulating-like behavior as the energy difference between the bands becomes larger. In the lower panel (a) we plot the spectral functions on a logarithmic frequency scale. The narrowing of the $j_{3/2}$ quasiparticle peak and the decreasing $j_{1/2}$ spectral weight at the Fermi level are clearly observed. We note that for $\lambda/D = 10^{-3}$ and $\lambda/D = 10^{-1}$ the spectral weights are essentially zero.

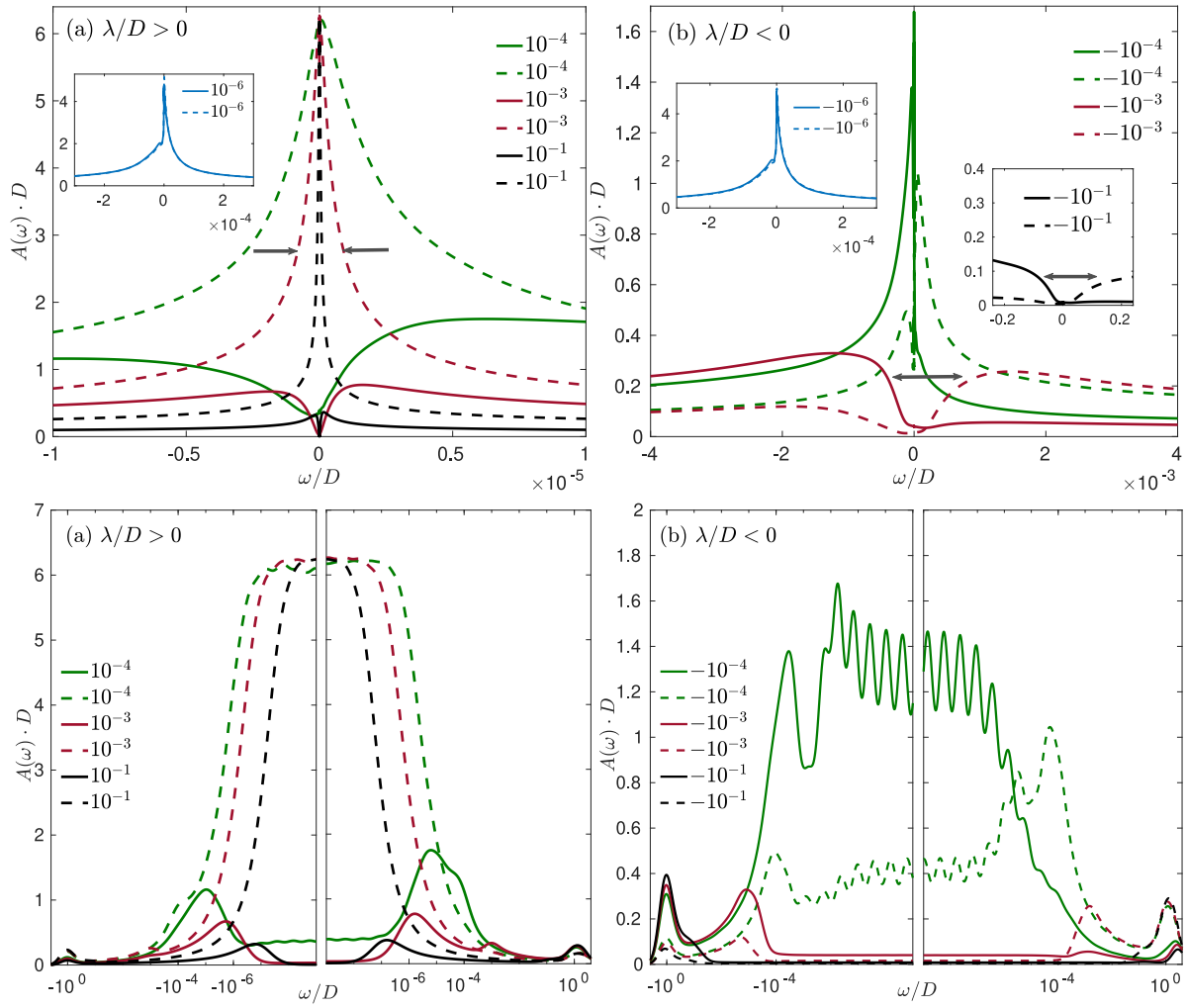

Figure 4.3: (Upper figures) Close-ups of the spectral functions at the Fermi level $\omega = 0$ for (a) $\lambda/D > 0$ and (b) $\lambda/D < 0$. The dashed lines refer always to $j_{3/2}$ states and the solid lines to $j_{1/2}$ states. In panel (a) we observe the narrowing of the $j_{3/2}$ spectral functions (as the grey arrows illustrate) and the small values of $j_{1/2}$ spectral functions. In the inset, we see the characteristically asymmetric shape of a Hund metal for $\lambda/D = 10^{-6}$. In panel (b) we observe the splitting of the initial quasiparticle coherent peak for $\lambda/D = -10^{-3}$ (and $\lambda/D = -10^{-1}$ in the right inset). (Lower figures) Spectral functions on a logarithmic frequency scale. Parameters: $n = 2, U/D = 3.2, J_H/D = 0.4, \Gamma \cdot D = 0.05, T \approx 0$.

For $\lambda/D < 0$ (upper panel (b)), we expect an insulating-like behavior for both bands.

In fact, for a filling of two electrons, the occupancy of $j_{1/2}$ states increases with SOC and the band approaches full filling. At the same time, the $j_{3/2}$ states become emptied out because of the large splitting. Interestingly, we observe a peak-like structure with large spectral weight around the Fermi level for both bands at the value $\lambda/D = -10^{-4}$, meaning that the j-structure is not dominant yet, whereas in the case of positive SOC (panel (a)) the spectral functions already have distinctive SOC-induced features. The SOC-induced effects set in clearly at $\lambda/D = -10^{-3}$ where both bands present an insulating-like behavior and the initial coherent quasiparticle peak (seen in the left inset for $\lambda/D = -10^{-6}$) is split by the SOC, with the splitting being of the order of the bands energy difference $\sim \lambda/D$. In the right inset the splitting and insulating-like behavior is also shown for $\lambda/D = -10^{-1}$. Looking at the spectral functions on a logarithmic frequency scale, lower panel (b), we observe a very wiggled behavior for $\lambda/D = -10^{-3}$ with relatively large spectral weight and then the splitting of order $\sim \lambda/D$ for $\lambda/D = -10^{-3}$ and $\lambda/D = -10^{-1}$ with nearly zero spectral weight. In particular, for $\lambda/D = -10^{-1}$ a Mott insulating state sets in.

We also plot the evolution of the occupancies $\frac{n_j}{2j+1}$ of the bands, see Fig. 4.4. For positive SOC, the $j_{3/2}$ states tend to the half-filling occupancy value 0.5, valid in the strong SOC limit, whereas the $j_{1/2}$ states become emptied out and the occupancy value approaches zero. We find that, at $\lambda/D = 0.1$ the $j_{3/2}$ occupancy is already around 80% of the strong coupling value. For negative SOC, the $j_{1/2}$ states tend to the fully occupied value 1, while $j_{3/2}$ states are emptied out. We find that, at $\lambda/D = -0.1$, the $j_{1/2}$ occupancy is already around 70% of the strong coupling value. Hence, for the parameters used, we observe strong SOC-induced effects already at $|\lambda|/D = 0.1$. In the spectral functions, Figs. 4.1, 4.2, we have observed clear effects of the SOC on the Hubbard bands at $|\lambda|/D = 10^{-4}$ and this is also seen in the orbital polarizations (difference in occupancies between the bands), which at $|\lambda|/D = 10^{-4}$ are found to be more than 30% of the full polarized values.

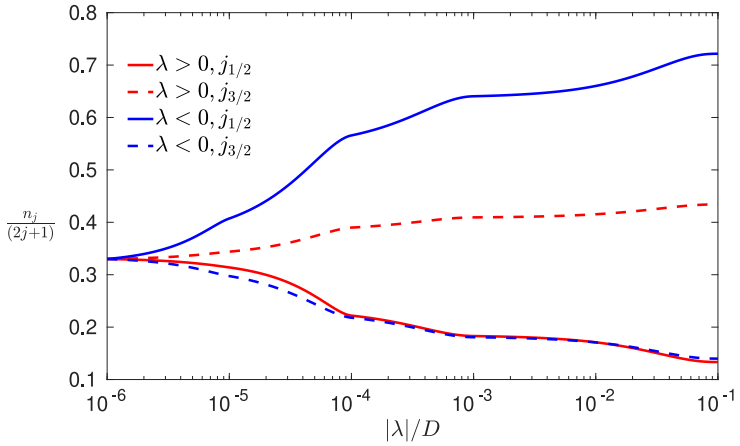

Figure 4.4: Evolution of the occupancies $n_j/(2j+1)$ of the $j_{1/2}$ and $j_{3/2}$ states for both signs of the SOC. With a filling of two electrons, the strong coupling values are 1 and 0.5 for $j_{1/2}$ and $j_{3/2}$ states, respectively. For $|\lambda|/D = 10^{-4}$ the polarization between the two bands is more than 30% of the full polarized value. Parameters: $n = 2, U/D = 3.2, J_H/D = 0.4, \Gamma \cdot D = 0.05, T \approx 0$.

We also compute susceptibilities as retarded correlators of bosonic operators A, B on the impurity as

$$\chi(t) = \langle A||B\rangle\,(t) = -i\,\Theta(t)\langle\,[A(t), B]\,\rangle\,, \tag{4.5}$$

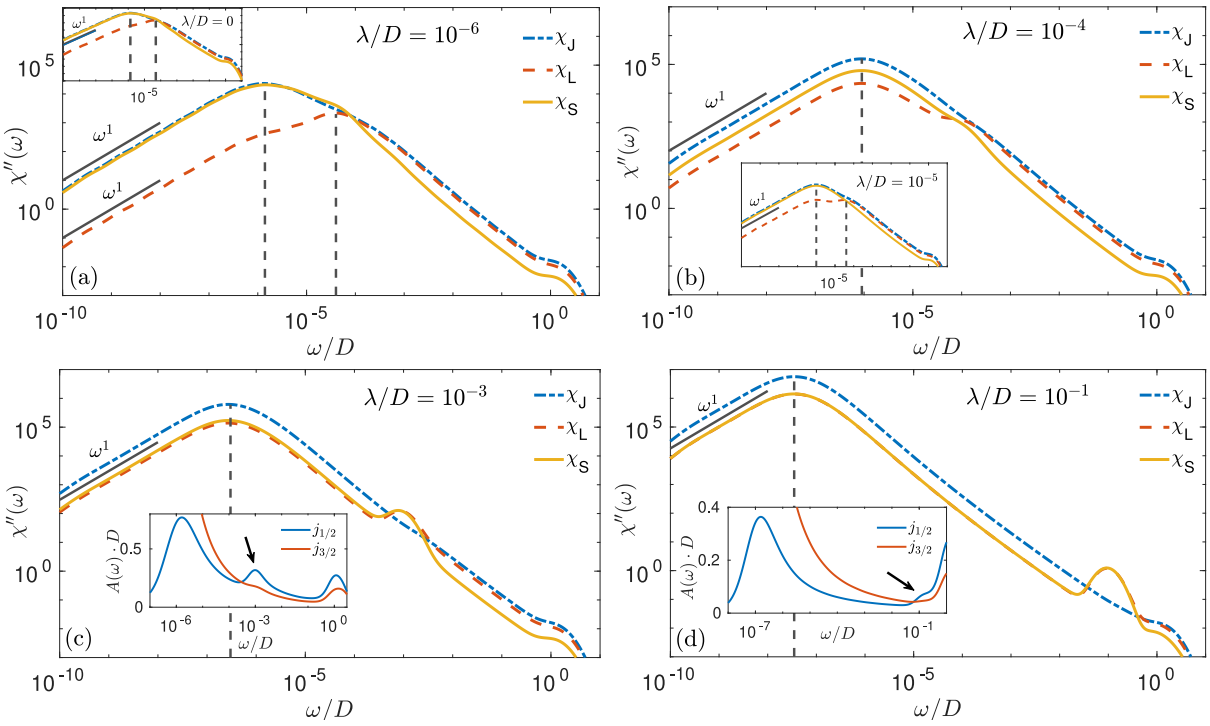

Figure 4.5: Spectral parts of susceptibilities for positive values of λ/D. In panel (a) and in the inset we observe the characteristic spin-orbital separation of Hund metals for 10^{-6} and for the case without SOC (Kondo scales indicated by dashed grey lines). In the inset of panel (b) the results for 10^{-5} show that SOC-induced effects are not visible yet, although there is a small bump in χ''_L at T_{sp} and a proper spin-orbital separation cannot be defined. For larger values of λ/D the spin separation is not present anymore. Insets of (c,d) show that the bumps seen in the susceptibilities are present also in the spectral functions. Once the spin fluctuations are screened we observe a Fermi-liquid linear behavior for all values, $\chi'' \sim \omega$ (solid grey lines). Parameters: $n = 2, U/D = 3.2, J_H/D = 0.4, \Gamma \cdot D = 0.05, T \approx 0$.

and we focus on the spectral part χ'' of the susceptibilities $\chi = \chi' - i\pi\chi''$, given by

$$\chi''(\omega) = \frac{1}{2\pi} \int dt\, e^{i\omega t} \langle\, [A(t), B]\, \rangle\, . \tag{4.6}$$

In fdmNRG we compute these susceptibilities via their Lehmann representation [58], for the total angular momentum $\mathbf{J}$, the total orbital angular momentum $\mathbf{L}$, the total spin $\mathbf{S}$ operators on the impurity,

$$\chi_J = \langle \mathbf{J} || \mathbf{J} \rangle_\omega\ , \quad \chi_L = \langle \mathbf{L} || \mathbf{L} \rangle_\omega \quad \chi_S = \langle \mathbf{S} || \mathbf{S} \rangle_\omega\ . \tag{4.7}$$

Hereafter we define the spin Kondo temperature T_K^{sp} and the orbital Kondo temperature T_K^{orb} as the energy scales where maxima of the spectral parts χ'' of the susceptibilities occur, after which the corresponding degrees of freedom begin to be screened by the bath electrons.

Let's look at the imaginary parts of the susceptibilities for positive SOC, see Fig. 4.5. As the spectral functions have shown, for $\lambda/D = 10^{-6}$ (panel (a)) SOC-induced effects are not clearly present yet and the typical spin-orbital separation of Hund metals is found [49, 7]. We see that χ''_J essentially concides with χ''_S at energies below T_K^{orb}, since the contribution from the orbital degrees of freedom is quenched. For the Kondo scales, we have $T_K^{orb} \approx 10^{-4}$ and $T_K^{sp} \approx 10^{-6}$. Since T_K^{sp} and λ/D have approximately the same

value, $\lambda/D = 10^{-6}$, one may argue that the SOC should already induce some effects. In the inset the case without SOC is shown, from which we see that the Kondo scales are equal to the case $\lambda/D = 10^{-6}$. Therefore, we do not observe SOC-induced effects for a strength comparable to the spin Kondo temperature T_K^{sp}. In the inset of panel (b) the results for $\lambda/D = 10^{-5}$ are shown, for which no clear SOC-induced effects are visible yet. The maximum of χ_L'' is still indicated although at lower energies χ_L'' increases again and its screening starts at T_K^{sp}. This signals the onset of weak SOC-induced effects and a spin-orbital separation cannot be properly defined. For $\lambda/D = 10^{-4}$ (panel (b)) the SOC sets in and remarkably the spin-orbital separation is not present anymore and both spin and orbital screenings occur at the spin Kondo scale $T_K^{sp} \approx 10^{-6}$. In panels (c,d), with $\lambda/D = 10^{-3}, 10^{-1}$, the absence of spin-orbital separation is also observed. The bumps of χ_L'' and χ_S'' at energies $\approx \lambda/D$ correspond to peaks in the spectral functions of the $j_{1/2}$ states, as seen in the insets. They could be numerical artifacts due to an overbroadening of discrete data but the origin of them is not clear yet. For all the values of SOC, once the spin fluctuations are screened, a Fermi-liquid linear behavior is observed, $\chi'' \sim \omega$. Note that, with increasing SOC, the susceptibilities have larger values and hence the process of screening begins at lower energies as the suppression of T_K^{sp} also shows. We have seen that the SOC induces a narrowing of the coherent peak, see Fig. 4.1. The lowering of T_K^{sp} seen in the susceptibilities supports this fact and the ensuing argument that the SOC makes the system more correlated.

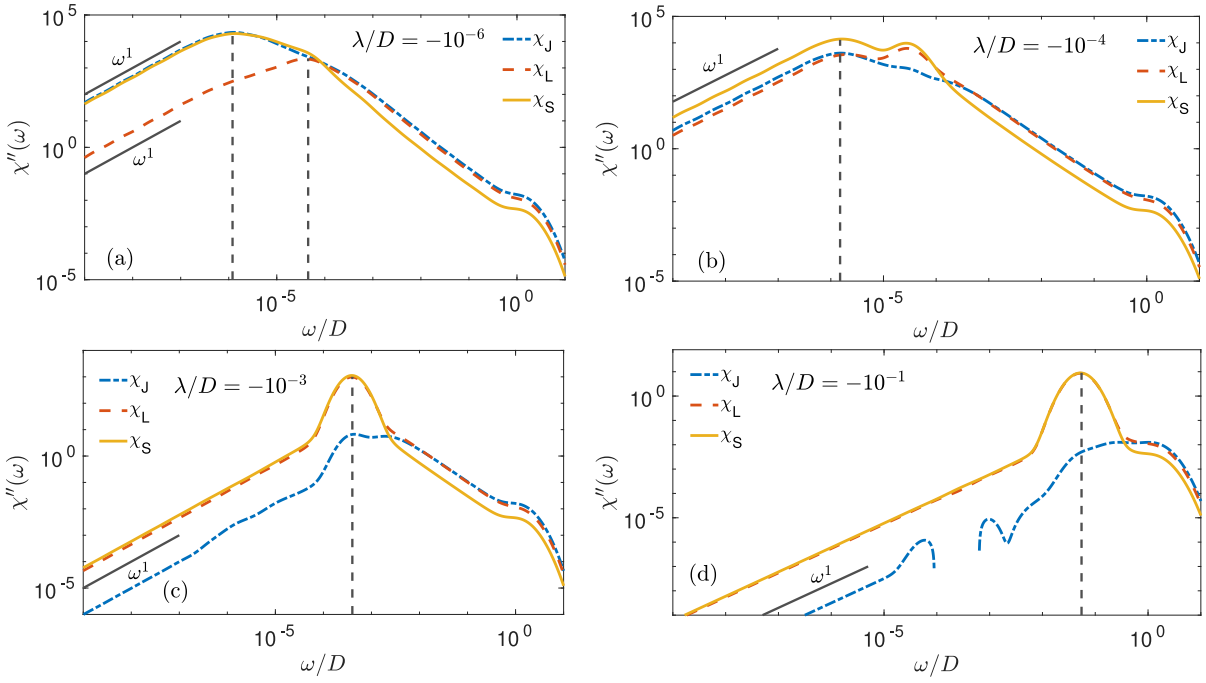

Figure 4.6: Spectral parts of susceptibilities for negative values of λ/D. In panel (a) we observe the characteristic spin-orbital separation of Hund metals for $\lambda/D = -10^{-6}$ (Kondo scales indicated by dashed grey lines). Panel (b) shows the results for $\lambda/D = -10^{-4}$, for which the spin separation is not present. Panels (c,d) show the results for $\lambda/D = -10^{-5}$ and $\lambda/D = -10^{-6}$, where we observe an insulating-like behavior with χ_J'' approaching very small values. Once the spin fluctuations are screened we observe a Fermi-liquid linear behavior for all values, $\chi'' \sim \omega$ (solid grey lines). Parameters: $n = 2, U/D = 3.2, J_H/D = 0.4, \Gamma \cdot D = 0.05, T \approx 0$.

Let's turn now to the case of negative SOC, see Fig. 4.6. For $\lambda/D = -10^{-6}$, panel (a), the results are essentially the same as in the positive-SOC case and we observe a spin-

orbital separation. For $\lambda/D = -10^{-5}$ the results also do not differ significantly from the positive-SOC case so they are not shown. In panel (b), for $\lambda/D = -10^{-4}$, the SOC sets in and the spin-orbital separation disappears and only one Kondo scale remains, at energies corresponding to the spin Kondo temperature $T_K^{sp} \approx 10^{-6}$, as in the positive-SOC case. In panel (c,d) we see the emergence of large peaks (likely numerical artifacts in this case) that possibly hide the maxima defining the Kondo scales. Were it the case, we note that T_K^{sp} would be pushed to higher energies at values $T_K^{sp} \approx \lambda/D$. This screening behavior has an atomic origin rather than involving the bath electrons. In fact for negative SOC, the spin and the orbital degrees of freedom tend to antialign (note that we have an extra minus sign from the T-P equivalence, Sec. 3.3.1), giving rise to a $J = 0$ state as soon as the energies are below the SOC scale. This is why we observe the behavior $T_K^{sp} \approx \lambda/D$, which therefore cannot be properly defined as T_K^{sp}, since it does not involve a screening process from the bath electrons. Indeed for $\lambda/D = -10^{-3}, -10^{-1}$ this $J = 0$ state is seen in the fact that χ''_J has very small values. For $\lambda/D = -10^{-1}$ (panel (d)) χ''_J has a negative value between $\lambda/D = -10^{-3}$ and $\lambda/D = -10^{-4}$, the origin of which is not clear. We conclude noting that, once the spin and orbital fluctuations are screened, the susceptibilities show a linear behavior, $\chi'' \sim \omega$, for negative SOC too.

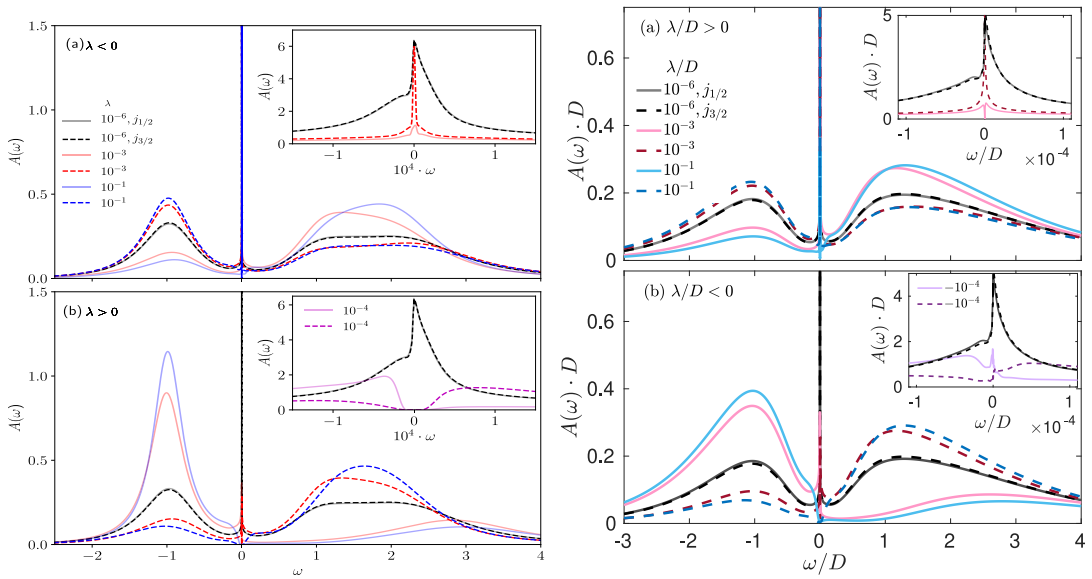

Figure 4.7: (a) Spectral functions from Ref. [16]; (b) Our results for spectral functions with same colours as in the Ref. [16]. Same parameters used: $n = 2, U/D = 3.2, J_H/D = 0.4, \Gamma \cdot D = 0.05, T \approx 0$.

As a check of our results, we compare the spectral functions with those obtained in Ref. [16], also using NRG with the same set of parameters, see Fig. 4.7.
We first note that the sign of SOC is inverted as it can be seen from the labels on the upper left corners. The reason is that we take the T-P minus sign into account in the Hamiltonian, while the authors of Ref. [16] do not change the sign of the SOC term in the Hamiltonian but consider an inverted Hund's third rule *a posteriori*. Taken this into account, the general structure of the spectral functions, in particular the transfer of spectral weights are in very good agreement, although they have different values of spectral weights since we divide each spectral function by the corresponding degeneracy (two for $j_{1/2}$ states and four for $j_{3/2}$ states). Comparing the upper insets, we observe similar

results, although the little bump in the pink curve of Ref. [16], which is a discretization artifact, is not present in our results. If we look at the lower insets, we note that, for the value $\lambda = 10^{-4}$ (purple curves), the results of Ref. [16] present the splitting of the coherent peak at $\omega = 0$, whereas in our results the splitting is not present yet and the spectral functions still have nonvanishing spectral weight. In our results the splitting is observed for $\lambda/D = 10^{-3}$, see panel (b) in Fig. 4.3.

An interesting question is to what scale the SOC should be compared in order to have relevant SOC-induced effects. Qualitatively, it is been argued that if the moments are screened at a higher scale than the SOC strength, the latter has nothing to act on [17]. For a Hund metal, where the onset of the orbital screening occurs at much higher energies than the spin screening, it is clear that one should compare the SOC to the orbital Kondo temperature T_K^{orb}. This qualitative argument has been backed by the numerical results of Ref. [16], where the authors computed static properties, as the effective local moment $\chi_J T$ versus temperature T, and the evolution of quantities with respect to λ, as the zero-temperature total angular momentum susceptibility $\chi_J(T = 0)$ and the occupancies (see [16]). They find that the SOC-induced effects indeed set in once the SOC is comparable to the zero-SOC value of the orbital Kond temperature T_K^{orb}. This claim is also supported by our results. The spectral functions show clear features of the j-orbital structure as well as the occupancies, for a value $\lambda/D \approx T_K^{orb} \approx 10^{-4}$. The dynamic susceptibilities, Figs. 4.5 and 4.6, also present SOC-induce effects, as the disappearance of spin-orbital separation, only when the SOC is comparable or larger than the zero-SOC value of T_K^{orb}, while we do not observe any effect related to the spin Kondo scale T_K^{sp}, see panel (a) and its inset, Fig. 4.5. However, the scale we estimate from the imaginary parts of dynamic susceptibilities is $T_K^{orb} \approx 10^{-4}$, whereas the estimated scale in Ref. [16] is $T_K^{orb} \approx 10^{-5}$, due to the fact that a definition of Kondo scales based on static susceptibilities is used (the temperature scales at which the local moments $T\chi_{S,L}$ drop below 0.07), see Fig. 4.8.

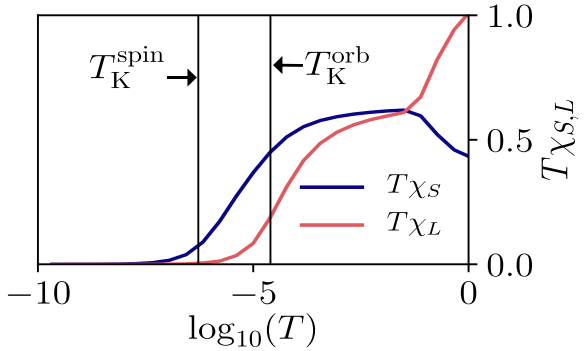

Figure 4.8: Local spin and orbital angular moments $T\chi_{S,L}$ from Ref. [16]. The temperature scales at which the local moments $T\chi_{S,L}$ drop below 0.07 define the spin and orbital Kondo temperatures. Parameters: $n = 2, U/D = 3.2, J_H/D = 0.4, \Gamma \cdot D = 0.05$.

In our NRG results, we have shown clear SOC-induced effects on spectral functions, reflecting the distinctive j-orbital structure obtained introducing the SOC. Interestingly, we have seen how the SOC induces the disappearance of the screening spin-orbital separation, a characteristic feature of Hund metals [49, 7]. Our results give support to the argument that the scale one should compare the SOC to is the orbital Kondo scale T_K^{orb}, determined at zero SOC. We also have checked the reliability of our results by comparing our spectral functions to those of Ref. [16] and found a very good agreement.

4.2 DMFT results

We now present the DMFT results. We adopt the Bethe lattice as noninteracting DOS, which leads to a closed form of DMFT self-consistent equations (Sec. 1.5) and take the half-bandwidth D of the DOS as unit of energy, $D = 1$. We initialize the DMFT self-consistency procedure with a metallic input hybridization and employ NRG as impurity solver, with the same computational details as in the previous section (Sec. 4.1). We keep the discretization parameter $\Lambda = 4$ but we vary the number of kept multiplets and the physical parameters. In the DMFT iterations the chemical potential is adjusted to obtain a filling per site of two electrons, $n = 2$. We perform the self-consistency procedure until convergence, i.e. $|\Gamma_{in}(\omega) - \Gamma_{out}(\omega)| \lesssim 10^{-3}$, which typically requires 4 DMFT loops. Our initial choice of parameters was inspired by real-materials values. In $3d$ systems the value of the Coulomb interaction is on the order of $U = 3-4\,eV$, the Hund coupling $J_H = 0.8-0.9\,eV$, the half-bandwidth $D = 1\,eV$ and the SOC $\lambda = 0.01-0.1\,eV$ ($\lambda = 0.07\,eV$ for Co) [2, 40]. In $4d$ systems the value of the Coulomb interaction is on the order of $U = 2-3\,eV$, the Hund coupling $J_H = 0.6-0.7\,eV$, the half-bandwidth $D = 1.5\,eV$ and the SOC $\lambda = 0.1-0.2\,eV$ ($\lambda = 0.13\,eV$ for Ru) [2, 40, 60, 44]. In $5d$ systems the value of the Coulomb interaction is on the order of $U = 1-2\,eV$, the Hund coupling $J_H = 0.4-0.5\,eV$, the half-bandwidth $D = 2\,eV$ and the SOC $\lambda = 0.3-0.5\,eV$ ($\lambda = 0.4\,eV$ for Ir) [40, 19, 60, 44]. We set $U/D = 3$, $J_H/D = 0.6$ and we vary λ/D in order to discuss our results in the context of $3d$ and $4d$ materials. We keep 8000 multiplets corresponding to ~ 40000 states.

Let's look at the spectral functions for $\lambda/D > 0$, Fig. 4.9. Note that we follow the same colour convention as in the NRG section for increasing value of SOC. We recall that for positive SOC the orbital structure consists of a lower-lying $j_{3/2}$ quadruplet and a higher-lying $j_{1/2}$ doublet. For the chosen parameters, the spectral functions are nearly degenerate for $\lambda/D = 10^{-4}$, meaning that the SOC-induce effects are not clearly present yet. As λ/D increases, the distinctive spectral weight transfer seen in the NRG results, Fig. 4.1, is not seen. Instead, the $j_{3/2}$ spectral functions seem to be quite insensitive to the SOC, as can also be seen on a logarithmic scale (lower panel). The $j_{1/2}$ states show asymmetric peaks near the Fermi level, which diminish and broaden with increasing SOC. Spectral weight transfer towards positive frequencies is found, signaling a smaller $j_{1/2}$ occupancy as expected from the orbital structure. The mentioned peaks are reminiscent of those seen in the NRG calculations for the susceptibilities, Fig. 4.5. From the analysis of the Hamiltonian eigenenergies they seem to not derive from atomic-like excitations though and their origin is not clear. Looking at the spectral functions on a logarithmic scale (lower panel), in contrast to NRG results, we do not observe any narrowing of the $j_{3/2}$ quasiparticle peak and the $j_{1/2}$ spectral weight near $\omega = 0$, although diminishing with increasing SOC, do not show the very small values, as seen in NRG results, see Fig. 4.3. Most unexpectedly the Hubbard bands are not present as we can seen in the linear-scale plot. To check if this is due to the SOC we plot the spectral functions without SOC (inset of panel (a)). Interestingly, a low and flat upper Hubbard band can be observed, but no lower band. Although the SOC could play a role, it is likely that the bands get overbroadened and suppressed during the self-consistency loop, for DMFT also enhances numerical artifacts. We will try to find out the reason of this disappearance at the end of the section.

Let's now turn to the spectral functions for $\lambda/D < 0$, Fig. 4.10. Now we have a lower-lying $j_{1/2}$ doublet and a higher-lying $j_{3/2}$ quadruplet. Also in this scenario the

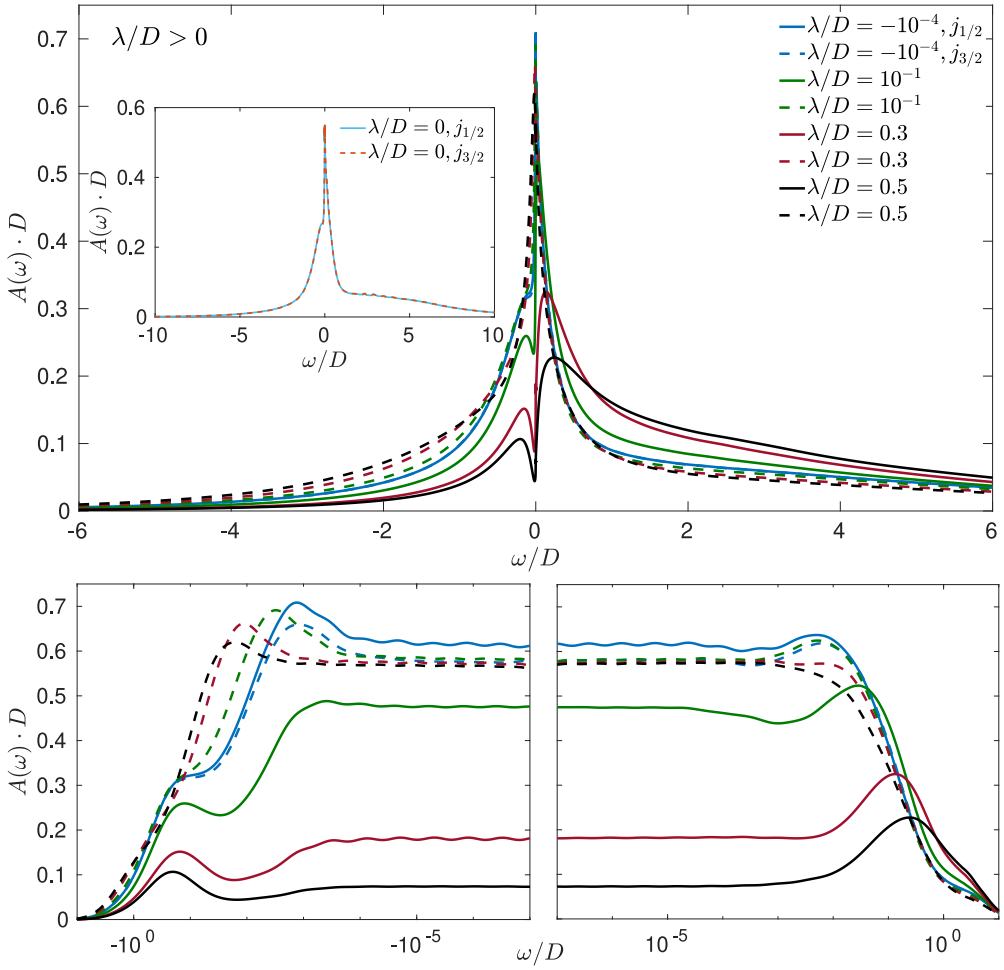

Figure 4.9: DMFT Spectral functions for positive SOC on a linear (upper) and logarithmic scale (lower). Parameters used: $n = 2, U/D = 3, J_H/D = 0.6, D = 1, T \approx 0$.

Hubbard bands are not observed. Here the spectral weight transfer induced by the SOC is visible, with the $j_{3/2}$ spectral weight pushed to positive energies while the $j_{1/2}$ spectral weight to negative ones, signaling a higher occupancy of the $j_{3/2}$ states. Further, note how the system approaches the strong-SOC band-insulator phase, with fully occupied $j_{1/2}$ states. Already for $\lambda/D = 0.5$ the $j_{1/2}$ spectral weight is very small at positive energies, signaling the suppression of charge fluctuations, while the $j_{3/2}$ spectral weight is very small at negative energies, meaning that the $j_{3/2}$ states become emptied out. Looking at spectral functions on a logarithmic scale (lower panel), one sees the diminishing of spectral weight for both bands near the Fermi level as in NRG, see Fig. 4.3, although no clear splitting of the quasiparticle peak occurs in the DMFT case.

In Fig. 4.11 we plot the real parts of the self-energie $\mathrm{Re}(\omega)$. For $\lambda/D > 0$ we observe that the SOC generally shifts upwards the curves. We find a characteristic inverted slope at small negative ω (also found in studies without SOC [35, 25]), which is enhanced with increasing SOC, especially for the $j_{1/2}$ states. We note that the $j_{3/2}$ curve (red) for $\lambda/D = 0.3$ does not present a pronounced inverted slope and its shape is qualitatively changed by the SOC. In the inset we compute the slope of $\mathrm{Re}(\omega)$ for the $j_{3/2}$ states, which gives valuable information about the quasiparticle weight, $Z = (1 - \partial_\omega \mathrm{Re}(\omega)_{\omega=0})^{-1}$, and hence about the degree of correlation of these states (the more negative the slope, the more correlated the states are). We find that the SOC actually makes these states less

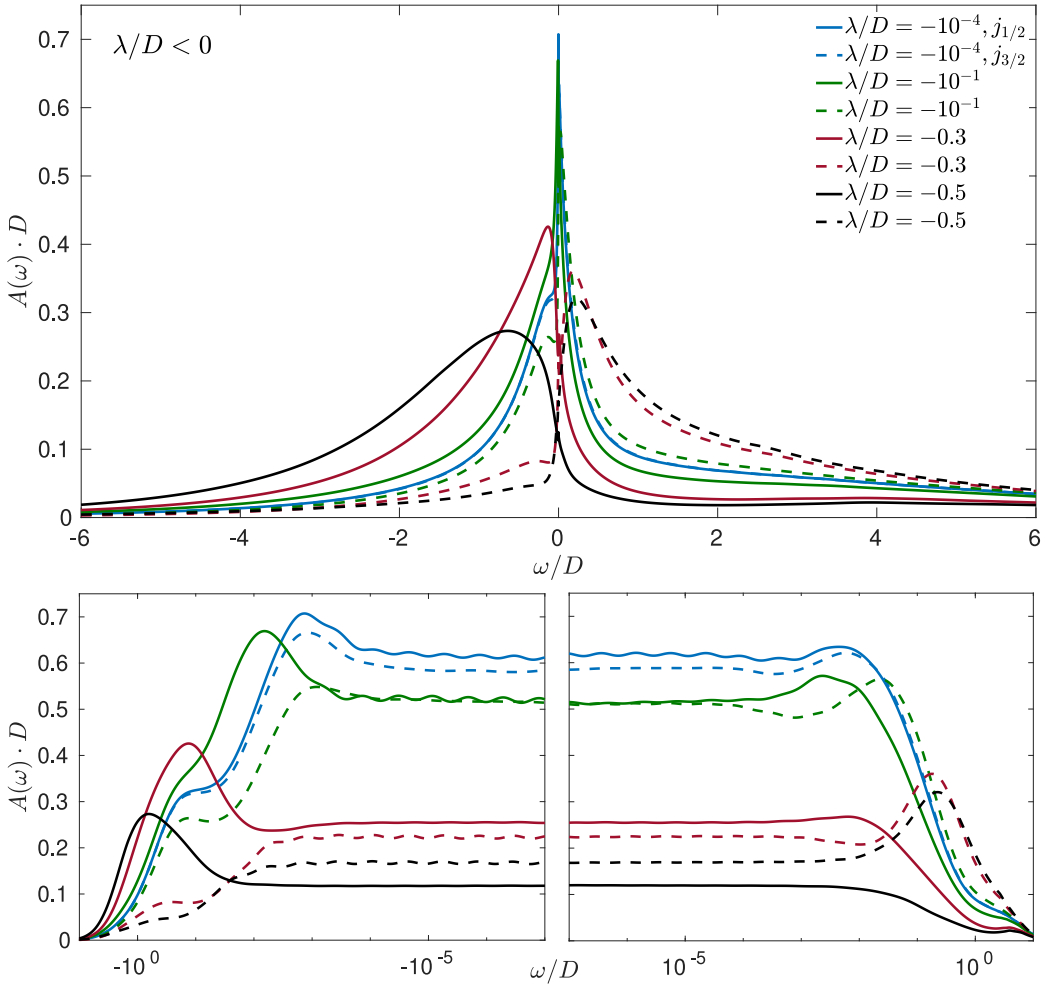

Figure 4.10: DMFT Spectral functions negative SOC (b) on a linear (upper) and logarithmic scale (lower). Parameters used: $n = 2, U/D = 3, J_H/D = 0.6, D = 1, T \approx 0$.

correlated, in contrast to what we observe in NRG calculations, see Fig. 4.3. In this sense the DMFT self-consistency is crucial to unveil how the SOC influences the physics of the model. This behavior was also found in a CTQMC study with an inverse temperature $\beta D = 80$ [52].

For negative SOC, panel (b), we see that the $j_{3/2}$ curves get pushed upwards by the SOC, whereas the $j_{1/2}$ curves downwards. We find less pronounced inverted slopes for $\lambda/D = 10^{-4}$ and $\lambda/D = 10^{-1}$ compared to the positive case. For $\lambda/D = 0.3$, the $j_{3/2}$ curve shows a broad and even less pronounced inverted slope, while it is not present for the $j_{1/2}$ curve. In the inset we plot the slopes of $\mathrm{Re}(\omega)$ for the $j_{3/2}$ states. We find a lesser degree of correlation due to the SOC in the negative case too.

Next, we analyze the imaginary parts of the self-energies, $-\mathrm{Im}(\omega)$, Fig. 4.12. Since the imaginary part of the self-energy is related to the real part by Kramers-Kronig relations, features corresponding to the inverted slopes of the real parts can be observed in the imaginary parts too (solid grey arrows). For both signs of SOC, the $j_{3/2}$ curves (dashed) are shifted by the SOC in a monotonic fashion, while for $j_{1/2}$ states the scenario is more complex with crossings for different values of SOC. For $\lambda/D > 0$ they occur for negative and positive frequencies, panel (a), while only for negative frequencies in the negative case, panel (b). The imaginary part of the self energy is related to the scattering rate (for a Fermi liquid the scattering rate is $\tau^{-1}(\omega) = -Z\,\mathrm{Im}\,\Sigma(\omega)$). In Figs. 4.12 we see

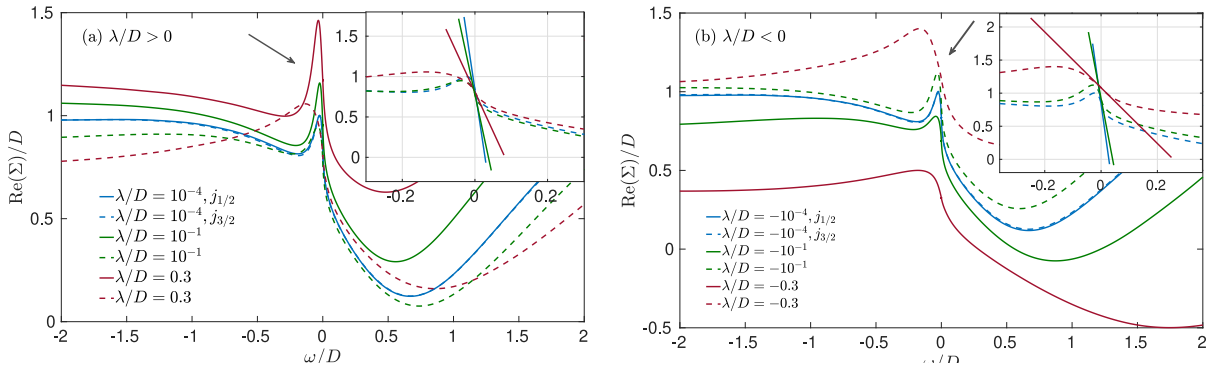

Figure 4.11: Real parts of the self-energy $\Sigma(\omega)$ for $\lambda/D > 0$ (a) and $\lambda/D < 0$ (b). Insets: slopes of $\mathrm{Re}(\omega)$ at $\omega = 0$ for the $j_{3/2}$ states, related to the quasiparticle weight, $Z = (1 - \partial_\omega \mathrm{Re}(\omega)|_{\omega=0})^{-1}$. Solid grey arrows indicate inverted slopes. Parameters used: $n = 2, U/D = 3, J_H/D = 0.6, D = 1, T \approx 0$.

that $-\mathrm{Im}(\omega)$ has larger values for positive frequencies than negative ones, for both signs of SOC. It follows that particle excitations have shorter lifetimes than hole excitations. In the insets, the $j_{3/2}$ curves are plot on a log-log scale, showing Fermi-liquid behavior $\mathrm{Im}\,\Sigma(\omega) \sim \omega^2$.

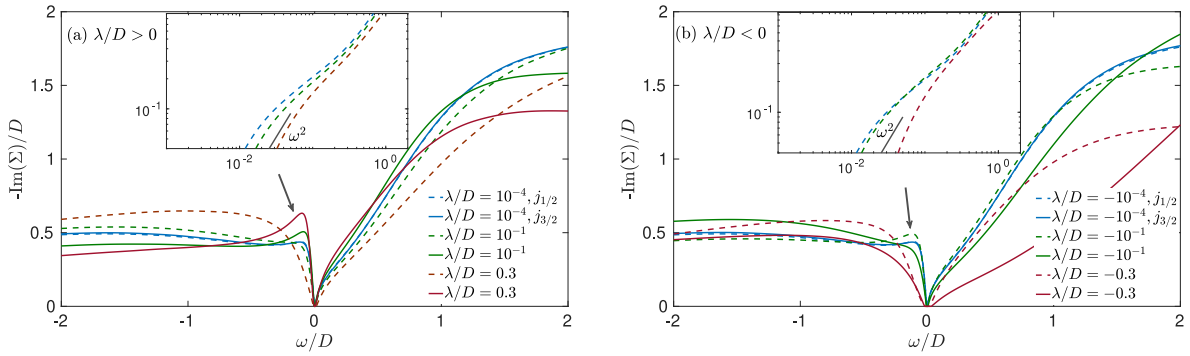

Figure 4.12: Imaginary parts of the self-energy $\Sigma(\omega)$ for $\lambda/D > 0$ (a) and $\lambda/D < 0$ (b). Insets: Fermi-liquid behavior near $\omega = 0$ at $T \approx 0$, $\mathrm{Im}(\omega) \sim \omega^2$. Parameters used: $n = 2, U/D = 3, J_H/D = 0.6, D = 1, T \approx 0$.

We now turn again to the disappearance of the Hubbard bands in the DMFT results. In order to single out the possible reason we vary the NRG parameters to see if some important differences in the spectral functions arise, see Fig. 4.13. The physical parameters used are the same, $n = 2, U/D = 3, J_H/D = 0.6, D = 1, T \approx 0$. In order to compare different settings we plot the spectral functions for $\lambda/D = \pm 10^{-1}$. In panel (a) we choose $\Lambda = 6$ and we keep the same number of multiplets as before, $N_k = 8000$. Compared to the case with $\Lambda = 4$, Fig. 4.9, we find similar features near $\omega = 0$ and no Hubbard bands, as expected for a larger Λ, yielding a coarser discretization, especially at higher energies. This is clearly seen in the inset where the case without SOC is plot. Compared to the $\Lambda = 4$ scenario (inset of panel (a) in Fig. 4.9), where a low and flat upper Hubbard band is observed, we do not see any clear sign of such a band. In panel (b) we plot results for a setting with $\Lambda = 8$ and $N_k = 12000$ kept multiplets. In this case we find less pronounced features near $\omega = 0$, slightly shifted spectral functions and still no Hubbard bands. We conclude that the disappearance of these bands, although intrinsically dependent of the

discretization parameter Λ, is not qualitatively due to computational details.

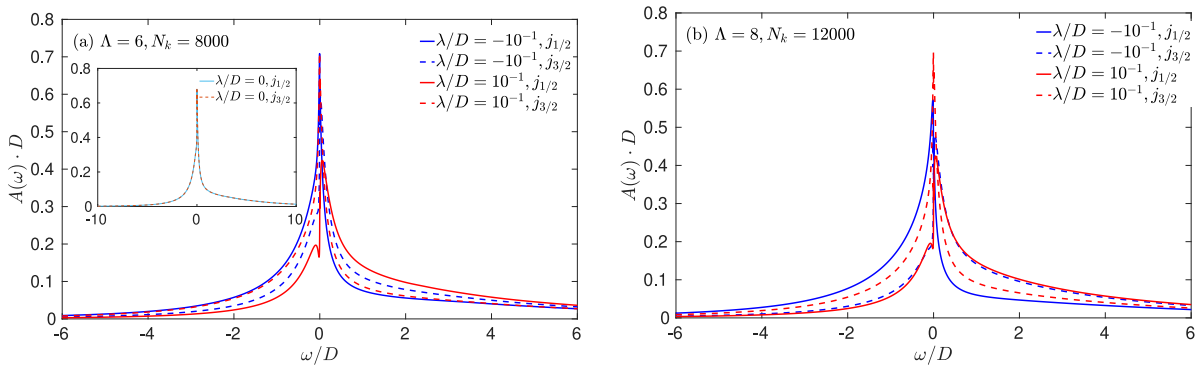

Figure 4.13: (a) Spectral functions with $\Lambda = 6$ and $N_k = 8000$ kept multiplets. (b) Spectral functions with $\Lambda = 8$ and $N_k = 12000$ kept multiplets. Parameters used: $n = 2, U/D = 3, J_H/D = 0.6, D = 1, T \approx 0$.

Recently we have reconsidered the physical parameters used in the calculations, motivated by real-materials values. In the NRG results, where Hubbard bands are clearly resolved, the formation of Hubbard bands is governed by the ratio $(U-3J_H)/(2D\Gamma)$, where $\Gamma = 0.05$ is the height of the box-shaped hybridization function. With a half-bandwidth $D = 1$, we obtain a normalization (area of the box-shaped hybridization function) of $2D\Gamma = 0.1$, while in the DMFT case with a semi-elliptical hybridization and $D = 1$ the normalization is 0.25. If we want a box-shaped hybridization matching the DMFT normalization, we need to set the height of the box to $\Gamma = \pi/8 \approx 0.393$. Then we estimate that for the original NRG calculation $(U/D = 3.2, J_H/D = 0.4, D = 1, \Gamma \cdot D = 0.05)$ the ratio $(U-3J_H)/(2D\Gamma) \approx 20$, while for the DMFT-normalized box hybridization function $(U/D = 3, J_H/D = 0.6, D = 1, \Gamma \cdot D = 0.393)$ the ratio $(U-3J_H)/(2D\Gamma) \approx 1.5$. This difference of one order of magnitude could explain why in the DMFT calculations the Hubbard bands are suppressed during the self-consistency loop. To verify this hypothesis we ran DMFT calculations with rescaled physical parameters so to have a similar ratio $(U-3J_H)/(2D\Gamma)$, namely $U/D = 6.4, J_H = 0.8$, always with the half-bandwidth $D = 1$ as unit of energy. The first results for this scenario have been obtained very recently. Therefore only partial results are available. The number of kept multiplets is $N_k = 6000$. The computed spectral functions are presented in Fig. 4.14. Finally we observe well-resolved Hubbard bands. In panel (a), we find that the j-bands are still degenerate for $\lambda/D = 10^{-4}$ while SOC-induced effects are present for $\lambda/D = 10^{-1}$, with a characteristic spectral weight transfer which reflects the orbital structure with the quadruplet $j_{3/2}$ lower in energy. For $\lambda/D = 10^{-4}$ the $j_{1/2}$ states have zero spectral weight at the Fermi level and $j_{3/2}$ states shows a narrowing of the quasiparticle peak, signaling less correlated states as found in the NRG results 4.3. In panel (b), $\lambda/D = -10^{-4}$ we do not observe SOC-induced effects on the quasiparticle peak while the Hubbard bands are not completely degenerate. For $\lambda/D = -10^{-1}$ the quasiparticle peak disappears and no splitting of order λ/D is seen, as in the NRG results. The system is in a Mott insulating phase.

We also plot the imaginary parts of the susceptibilities for $\lambda/D = 10^{-4}$ and $\lambda/D = 10^{-1}$. We observe spin-orbital separation for $\lambda/D = 10^{-4}$, with values of Kondo scales $T_K^{sp} \approx 10^{-3}$ and $T_K^{orb} \approx 10^{-2}$. For $\lambda/D = 10^{-1}$ the characteristic spin-orbital separation of Hund metals [49] is not present anymore and the onset of the screenings of spin and orbital fluctuations occur at the same energy scale, corresponding to the spin Kondo temperature

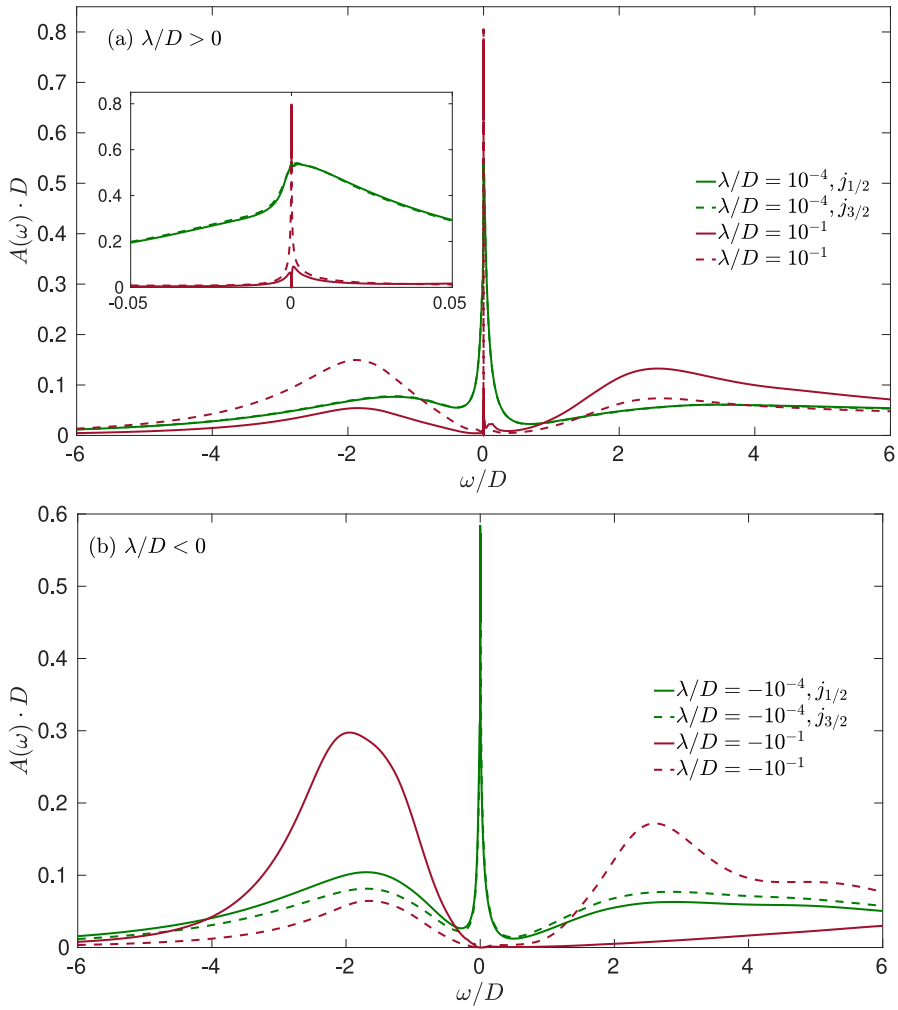

Figure 4.14: (a) Spectral functions for positive SOC, $\lambda/D = 10^{-4}$ and $\lambda/D = 10^{-1}$. Inset: spectral functions close-up at Fermi level $\omega = 0$. (b) Spectral functions with negative SOC, $\lambda/D = -10^{-4}$ and $\lambda/D = -10^{-1}$. Parameters used: $n = 2, U/D = 6.4, J_H/D = 0.8, D = 1, T \approx 0$.

$T_K^{sp} \approx 10^{-3}$, as found for the NRG results 4.5. Not having the results without SOC for this set of parameters we cannot verify though that the scale one should compare the SOC to is the bare orbital Kondo temperature T_K^{orb}, without SOC. Nonetheless we have verified that the spin-orbital separation also disappears in the DMFT results.

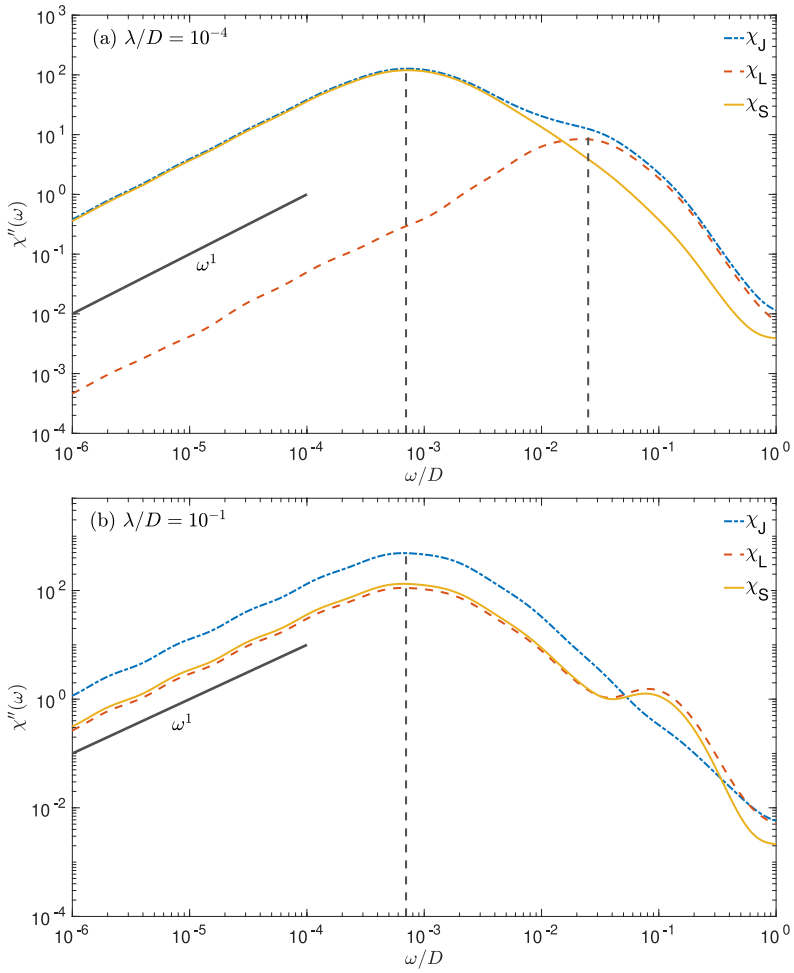

Figure 4.15: (a) Imaginary parts of the susceptibilities for $\lambda/D = 10^{-4}$. (b) Imaginary parts of the susceptibilities for $\lambda/D = 10^{-1}$. Dashed grey arrows indicate the Kondo scales. Once the fluctuations are quenched a Fermi-liquid linear behavior sets in, $\chi'' \sim \omega$. Parameters used: $n = 2, U/D = 6.4, J_H/D = 0.8, D = 1, T \approx 0$.

Conclusions

In this thesis we examined the effect of spin-orbit coupling (SOC) on the zero-temperature paramagnetic phase of a three-band Hubbard-Kanamori model, the complexity of which significantly increases with the introduction of the SOC. The three degenerate bands are split in two different flavours separated in energy. The spin and orbital symmetries are broken, in favor of the lower symmetry of the total angular momentum. The energy scales of electronic repulsion, Hund interaction, SOC and bandwidth are comparable and an intricate interplay arises. We focused on a filling of two electrons and changed the sign of the SOC to account for a filling of four electrons, since the SOC changes sign under particle-hole transformation.

To tackle the problem we employed the powerful NRG code available at Jan von Delft's group as an impurity solver for single-site DMFT. We first tested the code for the SOC-model on a quantum impurity problem without self-consystency. The results showed that the positive SOC increases the degree of correlation of metallic states and the negative SOC induces a Mott insulating state, adiabatically connected to a strong-SOC band insulator. We checked our computed spectral functions against those of Ref. [16] and found good agreement. We computed susceptibilities and found the disappearance of the spin-orbital separation for the onset of the screenings, a typical feature of Hund metals [49, 7]. Our results also supported the argument that the scale which determines the onset of SOC-induced effects is the bare orbital Kondo temperature [17, 16].

In the DMFT calculations we considered a set of parameters inspired by real-material values. We found that the positive SOC reduces the degree of correlation of metallic states in contrast to NRG calculations. For negative SOC no Mott phase is found. Notably, we did not observe Hubbard bands for a number of different computational settings. We then changed the physical parameters in relation to the those used in NRG calculations in order to find similar results. In this scenario Hubbard bands are resolved, along with other features also seen in the impurity results, such as enhanced correlations for positive SOC and Mott insulating phase for negative SOC. From preliminary results in this direction, we observed the closing of the spin-orbital separation region within DMFT as well.

To conclude, the SOC induces a rich range of effects on the physics of the model, particularly relevant for Hund metals. DMFT results show that the positive SOC enhances correlations for a certain set of parameters ($U/D = 3, J_H/D = 0.6$) but it reduces them in other regions of parameter space ($U/D = 6.4, J_H/D = 0.8$), as also found in [52]. Interestingly, both NRG and preliminary DMFT calculations show how the SOC closes the spin-orbital separation region, a fingerprint of Hund metals.

Let us discuss some possible future research topics in the field. Regarding our results, a detailed analysis of spin-orbital separation in relation to the onset scale of SOC-induced effects is certainly an interesting direction to pursue. Another fascinating topic would be to study thoroughly the influence of the SOC on correlations to derive a U vs J_H phase diagram. Another possibility is to study the problem for different fillings and see if

novel phases arise, as proposed in [21]. All in all, spin-orbit-coupled systems have drawn attention only recently and many research directions are possible.

Bibliography

[1] A. Georges, G. Kotliar, W. Krauth and M. J. Rozenberg, *Rev. Mod. Phys.* **68** (1996), 13–125.

[2] A. Georges, L. de' Medici, and J. Mravlje, *Annu. Rev. Condens. Matter Phys.* **4** (2013), 137.

[3] A.K. Mitchell, M.R. Galpin, S. Wilson-Fletcher, D.E. Logan, and R. Bulla, *Phys. Rev. B* **89** (2014), 121105.

[4] F. Anders and A. Schiller, *Phys. Rev. Lett.* **95** (2005), 196801.

[5] J.G. Bednorz and K.A. Müller, *Zeitschrift für Physik B Condensed Matter* **64** (1986), 189.

[6] D. Chandler: *Intoduction to Modern Statistical Mechanics*. Oxford University Press, 1987.

[7] X. Deng, K.M. Stadler, K. Haule, A. Weichselbaum, J. von Delft and G. Kotliar, *Nature Communications* **10** (2019), 2721.

[8] D.J. García, E. Miranda, K. Hallberg, and M.J. Rozenberg, *Phys. Rev. B* **75** (2007), 121102.

[9] E. Gull, A.J. Millis, A.I. Lichtenstein, A.N. Rubtsov, M. Troyer, and P. Werner, *Rev. Mod. Phys.* **83** (2011).

[10] L. Fanfarillo and E. Bascones, *Phys. Rev. B* **92** (2015), 075136.

[11] Gabriel Kotliar et al, *Phys. Rev. Lett.* **87** (2001), 186401.

[12] A. Georges and G. Kotliar, *Phys. Rev. B* **45** (1992), 6479–6483.

[13] H. R. Krishna-murthy, J. W. Wilkins, and K. G. Wilson, *Phys. Rev. B* **21** (1980), 1003.

[14] M. Hasan and C. Kane, *Rev. Mod. Phys.* **82** (2010), 3045.

[15] J. Hirsch and R. Fye, *Phys. Rev. Lett.* **62** (1986).

[16] A. Horvat, R. Žitko and J. Mravlje, *Phys. Rev. B* **96** (2017), 085122.

[17] J. Mravlje and A. Georges, *Phys. Rev. Lett.* **117** (2016), 036401.

[18] G. Jackeli and G. Khaliullin, *Phys. Rev. Lett.* (2009).

[19] J.G. Rau, E.K.-H. Lee, and H.-Y. Kee, *Annu. Rev. Condens. Matter Phys.* **7** (2016), 195.

[20] J. Kanamori, *Progress of Theoretical Physics* **30** (1963), 275.

[21] A.J. Kim, H.O. Jeschke, P. Werner and R. Valentí, *Phys. Rev. Lett.* **118** (2017), 086401.

[22] M. Kim, J. Mravlje, M. Ferrero, O. Parcollet and A. Georges, *Phys. Rev. Lett.* **120** (2018), 126401.

[23] K.M. Stadler, A.K. Mitchell, J. von Delft, and A. Weichselbaum, *Phys. Rev. B* **93** (2016), 235101.

[24] M. Kollar. *School on Correlated Electrons, DMFT: From Infinite Dimensions to Real Materials*. Forschungszentrum Jülich, 2018. Chapter: The Foundations of Dynamical Mean-Field Theory.

[25] F.B. Kugler, S.S.B. Lee, A. Weichselbaum, G. Kotliar and J. von Delft, *Phys. Rev. B* **100** (2019), 115159.

[26] L. Du, L. Huang, and X. Dai, *Eur. Phys. J. B* **86** (2013), 94.

[27] Y. Lu and M.W. Haverkort, *The European Physical Journal Special Topics* **226** (2017), 2549.

[28] M. Dzero, J. Xia, V. Galitski, and P. Coleman, *Annu. Rev. Condens. Matter. Phys* **7** (2016), 249.

[29] M. Imada, A. Fujimori, and Y. Tokura, *Rev. Mod. Phys.* **70** (1998), 1039.

[30] M. Yoshida, M. A. Whitaker, and L.N. Oliveira, *Phys. Rev. B* **41** (1990), 9403.

[31] W. Metzner, *Z. Physik B - Condensed Matter* **77** (1989), 253–266.

[32] W. Metzner and D. Vollhardt, *Phys. Rev. Lett.* **62** (1989), 324–327.

[33] M.H. Hettler et al., *Phys. Rev. B* **58** (1998), R7475.

[34] M.H. Hettler et al., *Phys. Rev. B* **61** (2000), 12739.

[35] J. Mravlje, M. Aichhorn, T. Miyake, K. Haule, G. Kotliar and A. Georges, *Phys. Rev. Lett.* **106** (2011), 096401.

[36] P. G. J. van Dongen, F. Gebhard and D. Vollhardt, *Z. Physik B - Condensed Matter* **76** (1989), 199–210.

[37] R. Bulla, A. C. Hewson, and Th. Pruschke, *Journal of Physics: Condensed Matter* **10** (1998), 8365.

[38] R. Bulla, T.A. Costi, and T. Pruschke, *Rev. Mod. Phys.* **80** (2008), 395.

[39] A.P. Ramirez, *Journal of Physics: Condensed Matter* **9** (1997), 8171.

[40] S. Maekawa, T. Tohyama, S.E. Barnes, S. Ishihara, W. Koshinbae, and G. Khaliullin: *Physics of Transition Metal Oxides*. Springer, Berlin, 2004.

[41] S.-S. B. Lee. Cumulative notes.

[42] S.-S. B. Lee and A. Weichselbaum, *Phys. Rev. B* **94** (2016), 235127.

[43] S. Sugano, Y. Tanabe, and H. Kamimura: *Multiplets of transition-metal ions in crystals*. Academic Press, 1970.

[44] R. Schaffer, E.K.H. Lee, B.J. Yang and Y.B. Kim, *Reports on Progress in Physics* **79** (2016), 094504.

[45] U. Schollwöck, *Ann. Phys.* **326** (2011).

[46] F. Schwabl: *Advanced Quantum Mechanics*. Springer, 2005.

[47] F. Schwabl: *Quantum Mechanics*. Springer, 2007.

[48] K.M. Stadler: *Towards exploiting non-abelian symmetries in the Dynamical Mean-Field Theory using the Numerical Renormalization Group*. Ludwig-Maximilians-Universität München, Master's Thesis, 2013.

[49] K.M. Stadler, Z.P. Yin, J. von Delft, G. Kotliar and A. Weichselbaum, *Phys. Rev. Lett.* **115** (2015), 136401.

[50] G.L. Stamokostas and G.A. Fiete, *Phys. Rev. B* **97** (2018), 085150.

[51] Y. Tokura and N. Nagaosa, *Science* **288** (2000), 462–468.

[52] R. Triebl, G.J. Kraberger, J. Mravlje and M. Aichhorn, *Phys. Rev. B* **98** (2018), 205128.

[53] D. Vollhardt. *School on Correlated Electrons, The LDA+DMFT approach to strongly correlated materials*. Forschungszentrum Jülich, 2011. Chapter: Dynamical Mean-Field Approach for Strongly Correlated Materials.

[54] E. Walter, K.M. Stadler, S.S.B. Lee, Y. Wang, G. Kotliar, A. Weichselbaum and J. von Delft, *arXiv:1908.04362* (2019).

[55] A. Weichselbaum, *Phys. Rev. B* **84** (2011), 125130.

[56] A. Weichselbaum, *Phys. Lett. B* **86** (2012), 245124.

[57] A. Weichselbaum, *Annals of Physics* **327** (2012), 2972.

[58] A. Weichselbaum and J. von Delft, *Phys. Rev. Lett.* **99** (2007), 076402.

[59] K.G. Wilson, *Rev. Mod. Phys* **47** (1975), 773.

[60] W. Witczak-Krempa, G. Chen, Y.B. Kim and L. Balents, *Annual Review of Condensed Matter Physics* **5** (2014), 57.

[61] Z.P. Yin, K. Haule, and G. Kotliar, *Nat. Mater.* **10** (2011), 932.

[62] R. Žitko, *Computer Physics Communications* **180** (2009), 1271.